CrossMark

SO Emission in the Dynamically Perturbed Protoplanetary Disks around CQ Tau and MWC 758

Francesco Zagaria[1,19] , Haochang Jiang[1,19] , Gianni Cataldi[2] , Stefano Facchini[3] , Myriam Benisty[1] , Yuri Aikawa[4] ,
Sean Andrews[5] , Jaehan Bae[6] , Marcelo Barraza-Alfaro[7] , Pietro Curone[8] , Ian Czekala[9] , Daniele Fasano[1,10] ,
Cassandra Hall[11,12] , Iain Hammond[1,13] , Jane Huang[14] , John D. Ilee[15] , Andrés F. Izquierdo[6,20] , Jensen Lawrence[7] ,
Giuseppe Lodato[3] , François Ménard[16] , Christophe Pinte[13,16] , Giovanni P. Rosotti[3] , Jochen Stadler[10] ,
Richard Teague[7] , Leonardo Testi[17] , David Wilner[5] , Andrew Winter[1,10] , and Tomohiro Yoshida[2,18]

[1] Max-Planck Institute for Astronomy (MPIA), Königstuhl 17, 69117 Heidelberg, Germany; frzagaria@mpia.de, h-jiang@mpia.de
[2] National Astronomical Observatory of Japan, 2-21-1 Osawa, Mitaka, Tokyo 181-8588, Japan
[3] Dipartimento di Fisica, Università degli Studi di Milano, Via Celoria 16, 20133 Milano, Italy
[4] Department of Astronomy, Graduate School of Science, University of Tokyo, Tokyo 113-0033, Japan
[5] Center for Astrophysics — Harvard & Smithsonian, 60 Garden St., Cambridge, MA 02138, USA
[6] Department of Astronomy, University of Florida, Gainesville, FL 32611, USA
[7] Department of Earth, Atmospheric and Planetary Sciences, Massachusetts Institute of Technology, Cambridge, MA 02139, USA
[8] Departamento de Astronomía, Universidad de Chile, Camino El Observatorio 1515, Las Condes, Santiago, Chile
[9] School of Physics & Astronomy, University of St. Andrews, North Haugh, St. Andrews KY16 9SS, UK
[10] Université Côte d'Azur, Observatoire de la Côte d'Azur, CNRS, Laboratoire Lagrange, 06300 Nice, France
[11] Department of Physics and Astronomy, The University of Georgia, Athens, GA 30602, USA
[12] Center for Simulational Physics, The University of Georgia, Athens, GA 30602, USA
[13] School of Physics and Astronomy, Monash University, Clayton, VIC 3800, Australia
[14] Department of Astronomy, Columbia University, 538 W. 120th St., Pupin Hall, New York, NY 10027, USA
[15] School of Physics and Astronomy, University of Leeds, Leeds, LS2 9JT, UK
[16] Univ. Grenoble Alpes, CNRS, IPAG, F-38000 Grenoble, France
[17] Alma Mater Studiorum Università di Bologna, Dipartimento di Fisica e Astronomia (DIFA), Via Gobetti 93/2, 40129 Bologna, Italy
[18] Department of Astronomical Science, The Graduate University for Advanced Studies, SOKENDAI, 2-21-1 Osawa, Mitaka, Tokyo 181-8588, Japan

Abstract

We report the serendipitous detection of the SO $J_N = 6_5$–5_4 (219.949 GHz) rotational transition in archival Atacama Large Millimeter/submillimeter Array observations of the spiral hosting protoplanetary disks around CQ Tau (with $\approx 4.9\sigma$ significance) and MWC 758 (with $\approx 3.4\sigma$ significance). In the former, the SO emission comes in the shape of a ring, arises from the edge of the continuum cavity, and is qualitatively consistent, at the currently available spectral resolution, with being in Keplerian rotation. In the latter, instead, while arising primarily from inside the continuum cavity, the SO emission also extends to the continuum ring(s), and its morphology and kinematics are less clear. We put these sources in the context of the other protoplanetary disks where SO detections have been previously reported in the literature and discuss the possible origins of SO in terms of (thermal) desorption or formation in the gas-phase. We argue that these processes might be fostered by dynamical perturbations caused by unseen embedded massive companions, shadows, or late-time infall, thus suggesting a possible link between perturbed dynamics and SO emission in (these) protoplanetary disks. If confirmed, our interpretation would imply that chemical evolution timescales could be significantly shorter in these systems than is commonly assumed, indicating that dynamical perturbations might influence the composition of newborn (proto)planets by altering the volatile makeup of their formation environment.

1. Introduction

High angular resolution observations of protoplanetary disks have revealed a wide variety of structures, offering indirect constraints on the physical mechanisms shaping them, such as planet–disk interactions (e.g., J. Bae et al. 2023) or (magneto) hydrodynamical instabilities (e.g., G. Lesur et al. 2023). At (sub)millimeter wavelengths, the most common features in the dust continuum are concentric gaps and rings (e.g., S. M. Andrews et al. 2018; F. Long et al. 2018; S. M. Andrews 2020). Molecular line observations often show analogous annular morphologies, reflecting a combination of temperature and abundance gradients that influence line intensities (e.g., K. I. Öberg & E. A. Bergin 2021; S. Facchini et al. 2021; K. I. Öberg et al. 2021). Sophisticated thermochemical models can reproduce many observed molecular line features, providing constraints on molecular abundances and the formation/ destruction pathways of volatile species (see K. I. Öberg et al. 2023; and references therein). However, besides a few notable exceptions (e.g., J. D. Ilee et al. 2011; H. Yoneda et al. 2016), these models most often considered disks to be dynamically unperturbed environments in a quasi-steady state, where chemical evolution occurs on secular timescales much

longer than the Keplerian orbital timescale (see K. I. Öberg et al. 2023).

In reality, it is increasingly evident that even in the class II stage protoplanetary disks might experience significant dynamical perturbations (e.g., J. Bae et al. 2023; C. Pinte et al. 2023) that can take place on short-enough timescales to give rise to (locally) active chemical processing. Additionally, even if chemical evolution were able to respond fast enough to such dynamical perturbations, thus relaxing back to a quasi-steady state, the local physical and chemical conditions under which chemical evolution would take place might still be substantially different from those typically assumed to forward-model the data (see, e.g., L. I. Cleeves et al. 2015; M. G. Evans et al. 2015, 2019; H. Jiang et al. 2023).

Observationally, some of the best examples of dynamically perturbed disks are those with spiral structures. In class II protoplanetary disks, spirals have been detected in dust thermal continuum, scattered-light emission, and in bright CO rotational line emission (see, e.g., L. M. Pérez et al. 2016; J. Huang et al. 2018; R. Teague et al. 2022; M. Benisty et al. 2023; L. Wölfer et al. 2023). Interestingly, spirals in scattered-light are often associated with azimuthally asymmetric structures in (sub)millimeter continuum emission (see, e.g., Y.-W. Tang et al. 2017; J. E. Pineda et al. 2019; H. Yang et al. 2023), possibly linked to long-lived anticyclonic vortices or horseshoes able to trap dust particles (N. van der Marel et al. 2021a).

Several hypotheses have been proposed to explain the possible origins of these spirals. A class of young sources, including IM Lup, Elias 2-27 (J. Huang et al. 2018; T. Paneque-Carreño et al. 2021), and AB Aur (J. Speedie et al. 2024), are often regarded as self-gravitating or under-going gravitational instability (GI; K. Kratter & G. Lodato 2016), as is supported by indirect kinematic evidence, such as (1) high dynamical masses (B. Veronesi et al. 2021), (2) GI-wiggles (C. Hall et al. 2020; C. Longarini et al. 2024; J. Speedie et al. 2024), in addition to, when present, (3) prominent continuum spirals, expected to be a telltale of self-gravity (K. Kratter & G. Lodato 2016).

Another popular interpretation involves (sub)stellar companions launching Lindblad spirals that propagate at sonic velocities within the disk (see, e.g., R. Dong et al. 2015; J. Bae & Z. Zhu 2018). However, while clear connections between the presence of close companions and spiral features can be made in some cases (e.g., HD 100543 and HD 142527, J.-F. Gonzalez et al. 2020; H. Garg et al. 2021), most of the planet-mass companions proposed to explain prominent spiral structures (such as those in MWC 758 and HD 169142, e.g., R. Dong et al. 2018; B. Ren et al. 2020; I. Hammond et al. 2023) remain debated. Conversely, PDS 70, the only disk with confirmed planet-mass companions (M. Keppler et al. 2018; S. Y. Haffert et al. 2019), does not show any clear spiral features.

Alternative explanations involve azimuthal disk temperature variations, such as those caused by shadows induced by a misaligned inner component or a warped disk (e.g., M. Montesinos et al. 2016; Z. Su & X.-N. Bai 2024; Z. Zhu et al. 2025; A. Ziampras et al. 2025), or infalling material from the surrounding environment (e.g., C. Ginski et al. 2021; D. Mesa et al. 2022; J. Huang et al. 2023), that can generate spiral-like structures within disks (e.g., G. Lesur et al. 2015; P. Hennebelle et al. 2017; M. Kuffmeier et al. 2020; A. Kuznetsova et al. 2022; J. Calcino et al. 2025).

All these mechanisms are expected to generate strong dynamical perturbations that can lead to (1) local temperature enhancement via viscous heating or the generation of shocks/compression (e.g., T. Ono et al. 2025), (2) an increase in the relative dust particle velocities, which makes ice-coated grains more susceptible to (potentially destructive) collisions (L. E. J. Eriksson et al. 2025), and (3) enhanced local turbulence that stirs solids into the warm, UV-illuminated upper disk layers (J. Bi et al. 2021; F. Binkert et al. 2023). These processes create favorable conditions for the release of volatiles, such as H_2CO, SO, and other oxygen-bearing species, into the gas-phase through direct thermal desorption or dust shattering, and their formation in the gas-phase via chemical reactions driven by energetic radiation (e.g., T. Aota et al. 2015). More generally, these perturbations would break the quasi-steady state of the disk, fostering active chemical processing. In this sense, it is no surprise that tracers like SO have been robustly identified in several spiral- and candidate-planet-hosting protoplanetary disks, such as HD 100546 (A. S. Booth et al. 2021, 2024a), AB Aur (A. Dutrey et al. 2024; J. Speedie et al. 2025), HD 169142 (A. S. Booth et al. 2023b; C. J. Law et al. 2023), and TW Hya (T. C. Yoshida et al. 2024).

In this work, we explore the possible link between the dynamical state of the disk and SO chemistry. We report the serendipitous detection of SO in archival Atacama Large Millimeter/submillimeter Array (ALMA) observations of the dynamically perturbed protoplanetary disks around CQ Tau and MWC 758. We put them in the context of the other class II sources where SO detections were previously published, discussing different possible origins for SO emission. In Section 2, we introduce these two systems, describe the available data sets that cover the SO $J_N = 6_5$–5_4 transition, and their self-calibration. Our new SO detections, their morphology, kinematics, and connections with scattered-light observations are presented in Section 3. Our results are discussed in the broader context of the other SO-bearing class II protoplanetary disks in Section 4. In Section 5, we summarize our results and draw our conclusions.

2. Sources, Data, Self-calibration

2.1. The Perturbed CQ Tau and MWC 758 Disks

CQ Tau—$M_\star = 1.47 \pm 0.18 M_\odot$ (M. Vioque et al. 2018), $d = 149.4 \pm 1.3$ pc (Gaia Collaboration 2020), SpT F2 (R. Garcia Lopez et al. 2006)—and MWC 758—$M_\star = 1.56 \pm 0.11 M_\odot$ (M. Vioque et al. 2018), $d = 155.9 \pm 0.8$ pc (Gaia Collaboration 2020), SpT A8 (S. L. A. Vieira et al. 2003)—are two Herbig stars located in the nearby HD 35187 association, near the Taurus star-forming region (K. L. Luhman 2023).

Thanks to their close proximity and high luminosity, the planet-forming disks around CQ Tau and MWC 758 are among the best-studied ones across a broad range of frequencies. Observations at (sub)millimeter wavelengths, first with the Submillimeter Array (SMA; A. Isella et al. 2010; A. Tripathi et al. 2017) and later with the ALMA, revealed the presence of (1) extended ($R_{1.3mm} \approx 66$ and 92 au, respectively) continuum emission with a ringlike morphology around wide ($R_{cav,mm} \approx 50$–60 au) and dust-depleted cavities (Y. Boehler et al. 2018; R. Dong et al. 2018; M. G. Ubeira Gabellini et al. 2019; P. Curone et al. 2025), and (2) larger-scale ($R_{CO} \approx 200$ and 300 au, respectively, M. Galloway-Sprietsma et al. 2025)

CO emission with smaller but still well-resolved ($R_{\mathrm{cav,CO}} \approx$ 30–50 au) cavities in ^{13}CO and C^{18}O emission (Y. Boehler et al. 2018; M. G. Ubeira Gabellini et al. 2019; L. Wölfer et al. 2021, 2023).

Both sources show telltale signatures of ongoing dynamical perturbations, as evidenced by their prominent scattered-light spiral structures, characterized by a dominant two-arm pattern with additional smaller-scale features (e.g., M. Benisty et al. 2015; I. Hammond et al. 2022; B. B. Ren et al. 2023), and their highly asymmetric (sub)millimeter continuum emission with two prominent bright arcs on top of a highly substructured wide ring on opposite sides of their cavity rims (Y. Boehler et al. 2018; R. Dong et al. 2018; M. G. Ubeira Gabellini et al. 2019), roughly aligning with the bases of the scattered-light spirals. Moreover, the cavity of MWC 758 shows a significant eccentricity of $e \approx 0.1$ (R. Dong et al. 2018; I. H. G. Kuo et al. 2022), further suggesting active dynamical sculpting.

Additionally, ^{12}CO observations revealed strong spiral structures in the kinematics of CQ Tau (L. Wölfer et al. 2021, 2023) and MWC 758 (L. Wölfer et al. 2025). These spirals are evident in the velocity residuals obtained after subtracting a Keplerian model from the line centroid maps (as done by A. F. Izquierdo et al. 2022; see M. Benisty et al. 2025, in preparation; L. Wölfer et al. 2025). Their magnitude is comparable to the local sound speed, consistently with the expectations for propagating sound waves, albeit likely a lower limit, due to the limited angular and spectral resolution of the available data.

2.2. Data and Self-calibration

We collected from the ALMA archive all the publicly available data of CQ Tau and MWC 758 that cover the SO $J_N = 6_5$–5_4 rotational transition at 219.949 GHz (Band 6). CQ Tau observations were conducted in Cycles 2, 4, and 5 between 2015 August and 2017 November, as part of the programs 2013.1.00498.S (PI: L. Pérez), 2016.A.00026.S (PI: L. Testi), and 2017.1.01404.S (PI: L. Testi). MWC 758 was observed in Cycle 5 as part of the program 2017.1.00940.S (PI: L. Ricci) between 2017 October and December. The observational setup details are summarized in Appendix A.

The data were first pipeline calibrated by the ESO node of the European ALMA Regional Centre, and then self-calibrated using the software Common Astronomy Software Applications (CASA; see The CASA Team et al. 2022) v6.6.5-31, following the procedure adopted by the DSHARP[21] (S. M. Andrews et al. 2018), MAPS[22] (I. Czekala et al. 2021), and exoALMA[23] (R. A. Loomis et al. 2025) collaborations. A detailed description of the self-calibration procedure can be found in Appendix B. We measured a peak signal-to-noise ratio (SNR) of $\approx$90 and $\approx$170 in our fiducial continuum images of CQ Tau and MWC 758. Their rms noise is within 24.3% and 91.6% of the expected thermal noise as estimated using the apparent-sens[24] (CASA task), indicative of some residual phase noise at high angular resolution. The self-calibrated and continuum-subtracted data sets were used to generate SO emission cubes (at the highest achievable spectral resolution of 0.7 km s^{-1} for CQ
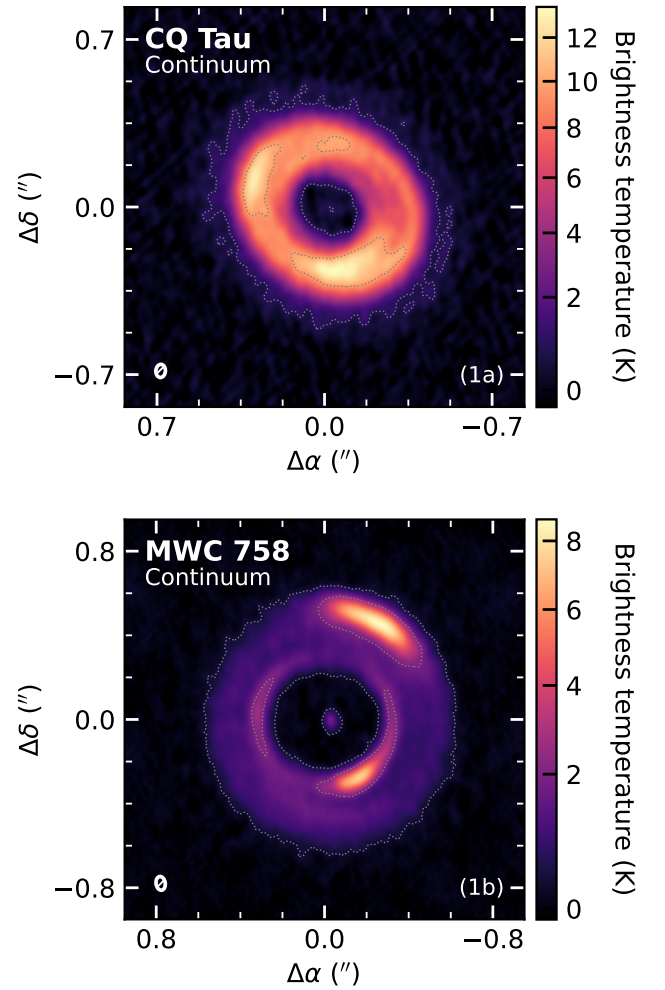

Figure 1. 1.3 mm continuum emission map of CQ Tau (top) and MWC 758 (bottom). The dotted gray lines highlight the [5, 65] $\times \sigma$ (CQ Tau) and the [5, 40] $\times \sigma$ (MWC 758) emission contours. The ellipse in the bottom left corner of each panel displays the synthesized CLEAN beam.

Tau, and 1.4 km s^{-1} for MWC 758) and moment maps, as is detailed in Appendix C.

3. Results

Continuum emission. The continuum emission maps reconstructed with our fiducial imaging parameters (Appendix C for the details) are shown in panels (a) and (b) of Figure 1. Here and in the following figures, the brightness temperature is computed in the Rayleigh–Jeans approximation. The dotted gray lines display the [5, 65] $\times \sigma$ and the [5, 40] $\times \sigma$ emission contours. These values were chosen to highlight the location of the cavity rim and the continuum crescents. As previously discussed by M. G. Ubeira Gabellini et al. (2019), Y. Boehler et al. (2018), R. Dong et al. (2018), and P. Curone et al. (2025), in both sources, the continuum morphology is characterized by (1) a deep, almost empty (and, in MWC 758, also clearly eccentric) cavity with a faint inner disk, and (2) bright crescent-like asymmetries on top of a wide, potentially substructured, continuum ring, suggestive of strong dynamical perturbations (as is highlighted in the highpass continuum and scattered-light images shown in Appendix C).

SO emission. SO emission is detected both in CQ Tau and in MWC 758 as is clear from the shifted and stacked spectra (blue

---

[21] https://almascience.eso.org/almadata/lp/DSHARP/

[22] https://alma-maps.info/overview.html

[23] https://www.exoalma.com/

[24] https://casadocs.readthedocs.io/en/stable/api/tt/casatasks.imaging.apparentsens.html
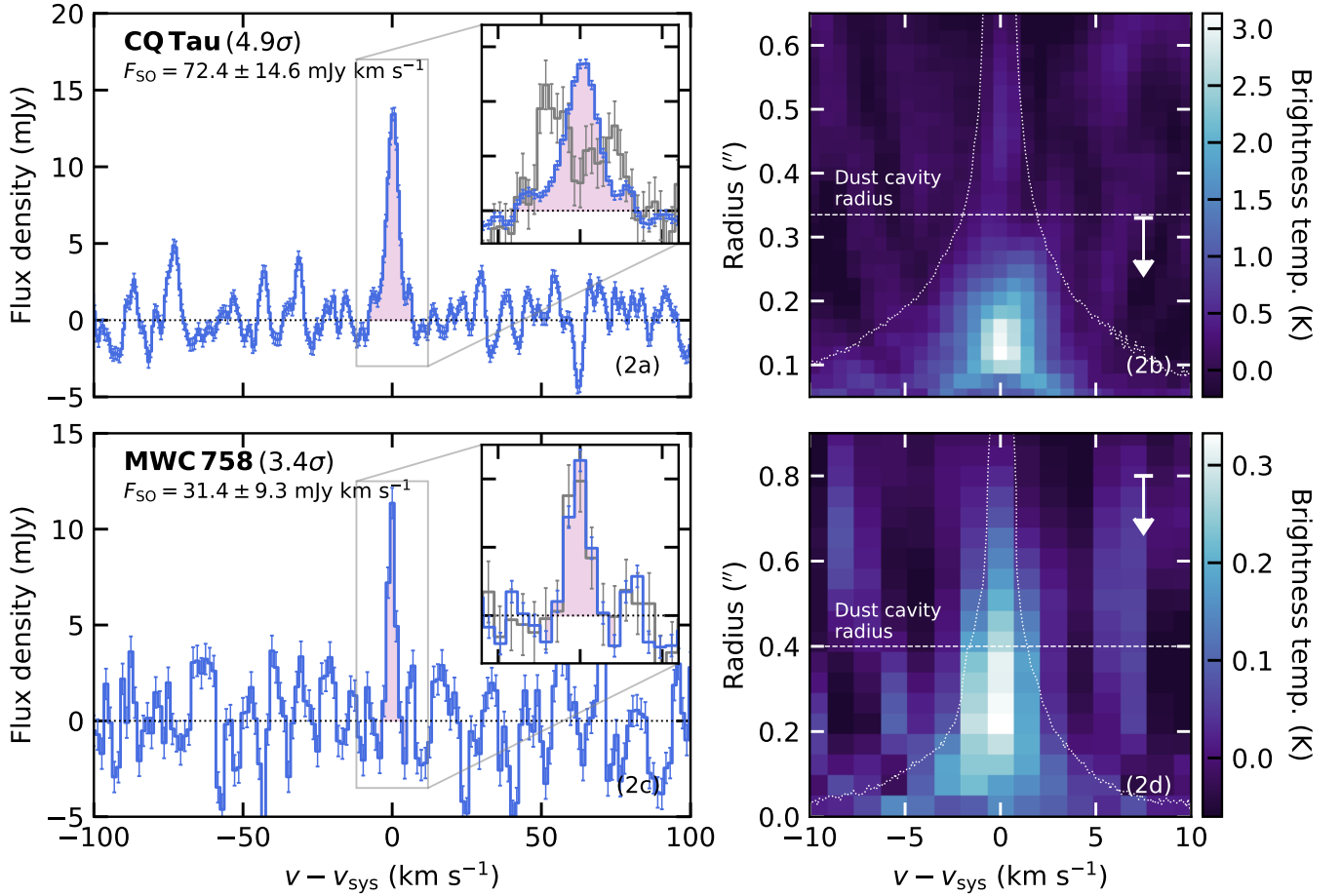
Figure 2. Left: shifted and stacked SO spectra (blue). The zoom-in inserts around the systematic velocity also display the native spectra (gray) for comparison. The plum areas highlight the velocity ranges adopted to measure the SO flux and generate moment maps (see Appendix C). Right: teardrop plots. The dotted white lines mark the region where Keplerian emission from the disk is expected. Those correspond to the location where the CO emission (from the fiducial exoALMA cubes, R. Teague et al. 2025) drops below 3 K. The white arrows indicate the apertures over which the spectra were extracted and integrated over to measure the SO flux. The dust cavity radius is indicated with a white dashed line. SO emission is clearly detected and primarily originates within the cavity.

lines, panels (2(a) and (c)) and teardrop plots (panels 2(b) and (d)) displayed in Figure 2, both generated using gofish (R. Teague 2019), from our fiducial cubes (Appendix C for details), with fluxes of 72.4 ± 14.6 (4.9σ detection) and 31.4 ± 9.3 (3.4σ detection) mJy km s^{-1}, respectively. These line intensities were measured by integrating the shifted and stacked spectra extracted from a circular mask with a radius of 0."33 (CQ Tau) and 0."80 (MWC 758). These apertures correspond to the disk radius where the cumulative distribution of the SO emission, obtained by integrating the shifted and stacked spectra extracted from progressively larger circular masks, flattens out (see the arrows in the teardrop plots in panels (2(b) and (2d)). The flux uncertainties, instead, were estimated as the standard deviation of the fluxes measured by integrating the shifted and stacked spectra in nonoverlapping spectral ranges as wide as those used to measure the line intensities (to take into account the spectral correlation across channels induced by line shifting and stacking), but not covering the SO transition, extracted from the same disk region.

Figure 3 displays the SO integrated intensity (panels (3a) and (3e)), peak intensity (panels (3b) and (3f)), and velocity ("moment 1," panels (3c) and (3g)) maps, generated using bettermoments (R. Teague & D. Foreman-Mackey 2018), without applying any channel or threshold clipping, for our fiducial CLEANing parameters. In addition, a comparison

between SO peak intensity and scattered-light morphology is displayed in panels (3d) and (3h). Some relevant channel maps, reconstructed with the same fiducial parameters, are shown in Appendix C.

In CQ Tau, SO is detected with high (5σ–10σ) significance across several independent channels (see Appendix C). The integrated intensity map indicates that SO emission primarily arises from the edge of the continuum cavity (as is suggested by the teardrop plot in Figure 2) in the form of a ring, with a small inner gap and a bright spot in the direction of the southeast crescent (on the far side of the disk). The SO peak intensity map is also brighter at the cavity rim. However, its morphology is not ringlike, but asymmetric and brighter along the disk major axis and azimuthally closer to the continuum crescents. The comparison between the SO peak intensity emission morphology and the K_s-band Q_ϕ polarized differential image of B. B. Ren et al. (2023), displayed in panel (3d), suggests that the SO emission is preferentially colocated with the innermost regions of the scattered-light spiral wakes. While, at a first glance, this alignment might suggest a common dynamical origin for the scattered-light spirals and the SO emission, we caution that their colocation is not necessarily physical, as is indicated by the morphological differences between integrated and peak intensity maps, and could be a consequence of limb brightening. In fact, due to a
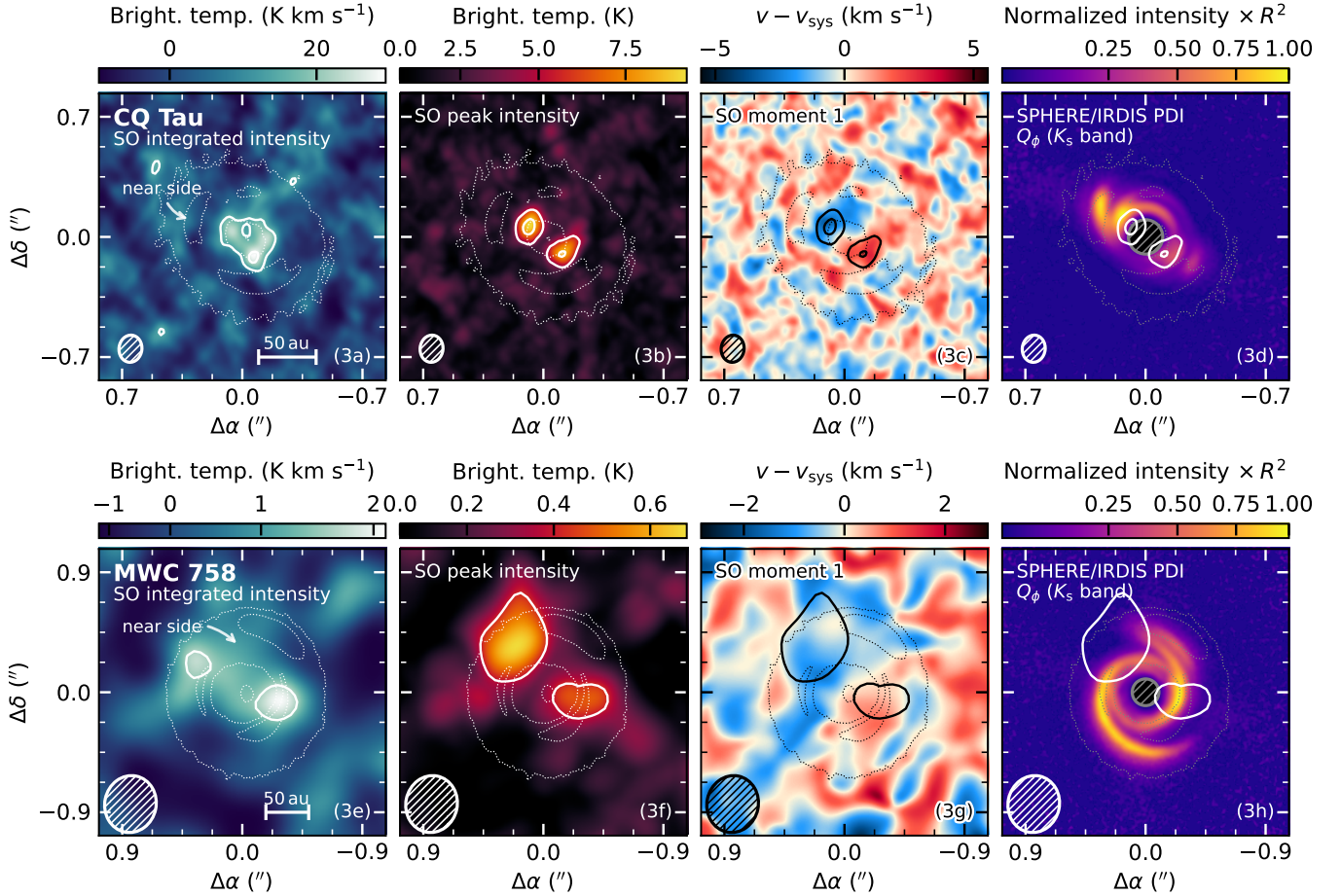
Figure 3. From left to right: SO integrated intensity ("moment 0"), peak intensity ("moment 8"), velocity ("moment 1") maps, and comparison between scattered-light images and SO peak intensity for CQ Tau (top row) and MWC 758 (bottom row). The dotted contours display the $[5, 65] \times \sigma$ (CQ Tau) and the $[5, 40] \times \sigma$ (MWC 758) emission levels. The white (black for panels (3c) and (3g)) solid contours, instead, mark the $[3, 5] \times \sigma$ SO detection levels. The synthesized CLEAN beam is shown as an ellipse in the bottom left corner of each panel. The regions within 0″.1 of the scattered-light images cannot be accessed because of the coronagraph and are masked out.

combination of the potentially low optical depth of SO (see, e.g., the $C^{18}O$ integrated intensity map in PDS 70, C. J. Law et al. 2024) and the limited resolution and sensitivity of our data set (e.g., L. Wölfer et al. 2021), emission from the higher velocity channels could be artificially enhanced along the disk minor axis. Finally, the SO velocity map (Figure 3, panel (3c)) indicates that, at the currently available spectral resolution (of $\approx 0.7 \, \mathrm{km \, s^{-1}}$), the SO emission is qualitatively compatible with Keplerian rotation. However, we cannot exclude lower-amplitude velocity perturbations (e.g., due to the presence of spirals; see, e.g., the CO velocity residuals published by A. F. Izquierdo et al. 2023, typically of order $\leqslant 0.4 \, \mathrm{km \, s^{-1}}$).

In MWC 758, SO is detected only in few independent channels with $>3\sigma$ significance (Appendix C), not only because of the lower source inclination but also possibly because SO emission is more extended but overall fainter. Both the SO integrated intensity and peak intensity maps (panels (e) and (f) of Figure 3) display two bright spots along the disk major axis and along the main ring, close to the continuum cavity edge (as was hinted by the teardrop plot in Figure 2). Similarly to CQ Tau, the SO emission velocity of MWC 758 (panel (3g)) is qualitatively consistent with being Keplerian. Finally, the comparison between SO peak intensity and the K_s-band Q_ϕ polarized differential image of B. B. Ren et al. (2023), displayed in panel (3h), does not show any connections between SO emission and scattered-light spirals.

4. Discussion

4.1. Comparison with the Other SO-bearing Class II Disks

We detected emission from the SO $J_N = 6_5-5_4$ transition in CQ Tau and MWC 758. With these two new sources, SO detections have been so far reported in nine class II disks: UY Aur (Y.-W. Tang et al. 2014), HD 100546 (A. S. Booth et al. 2018, 2023a, 2024a), IRS 48 (A. S. Booth et al. 2021, 2024b), HD 169142 (A. S. Booth et al. 2023b; C. J. Law et al. 2023), AB Aur (A. Fuente et al. 2010; S. Pacheco-Vázquez et al. 2016; P. Rivière-Marichalar et al. 2020; A. Dutrey et al. 2024; J. Speedie et al. 2025), DR Tau (J. Huang et al. 2023, 2024), TW Hya (T. C. Yoshida et al. 2024), and CQ Tau and MWC 758. Remarkably, six of these systems, including CQ Tau and MWC 758, (1) are around Herbig stars and (2) show large inner cavities in their ALMA continuum, ^{13}CO, and $C^{18}O$ emission. Moreover, their detected SO emission is consistently located inside or near the edge of these cavities.

We first checked for any correlations between SO emission and stellar properties in our sample of class II disks with SO detections. For disks lacking SO $J_N = 6_5-5_4$ observations, we estimated its flux based on the line flux of the detected transition with the closest upper state energy to the $J_N = 6_5-5_4$ one, and rescaled the fluxes to a common distance of 140 pc. Both the optically thin and thick regimes were considered, with the conversion process

Table 1
Stellar and Disk Properties of the Class II Sources with SO Detections

Source	$M_\star$ ($M_\odot$)	$\log_{10} L_\star$ ($L_\odot$)	$t_\star$ (Myr)	SpT	M_{dust} ($M_\oplus$)	$\log_{10}\dot{M}_{acc}$ ($M_\odot\,yr^{-1}$)	SO trans.	F_{SO} (mJy km s^{-1})	References
(1)	(2)	(3)	(4)	(5)	(6)	(7)	(8)	(9)	(10)
TW Hya	$0.9^{+0.1}_{-0.2}$	$-0.54^{+0.13}_{-0.10}$	$9.8^{+6.2}_{-1.4}$	M0.5	57.1 ± 0.1	-8.65 ± 0.22	7_8–6_7	13 ± 3	(1, 1, 1, 2, 3, 1, 4)
HD 100546	$2.06^{+0.10}_{-0.12}$	$1.37^{+0.07}_{-0.05}$	$5.5^{+1.4}_{-0.8}$	A0	38.0 ± 3.9	-6.95 ± 0.36	7_8–6_7	343 ± 26	(5, 5, 5, 6, 7, 8, 9)
AB Aur	$2.15^{+0.36}_{-0.21}$	$1.61^{+0.19}_{-0.21}$	$4.0^{+1.4}_{-1.5}$	A0	11.8 ± 1.2	-6.13 ± 0.27	6_5–5_4	330 ± 10	(5, 5, 5, 10, 7, 11, 12)
IRS 48	2.5	1.62	4.1	A0	7.8	-8.40 ± 0.50	7_8–6_7	1063 ± 23	(13, 13, 13, 14, 15, 16, 17)
HD 169142	2.00 ± 0.13	$1.31^{+0.12}_{-0.22}$	$9.0^{+11.0}_{-3.9}$	F1	22.9 ± 2.4	-7.09 ± 0.21	8_8–7_7	120 ± 10	(5, 5, 5, 6, 7, 11, 18)
UY Aur A	0.60	-0.49 ± 0.2	5.13	M0	11.2 ± 0.6	-7.64	6_5–5_4	N/A	(19, 19, 19, 19, 20, 19, 21)
UY Aur B	0.34	-0.77 ± 0.2	3.89	M2.5	4.4 ± 0.1	-7.70	6_5–5_4	N/A	(19, 19, 19, 19, 20, 19, 21)
DR Tau	$0.83^{+0.34}_{-0.24}$	-0.54 ± 0.20	$3.2^{+2.7}_{-1.4}$	K4	70.4 ± 0.1	-7.93 ± 0.40	6_5–5_4	195 ± 9	(22, 22, 22, 22, 20, 22, 23)
CQ Tau	$1.47^{+0.19}_{-0.11}$	$0.87^{+0.18}_{-0.12}$	$8.9^{+2.8}_{-2.5}$	F2	44.2 ± 4.8	<-8.33	6_5–5_4	72.4 ± 14.6	(5, 5, 5, 24, 7, 8, 25)
MWC 758	$1.56^{+0.11}_{-0.08}$	$1.04^{+0.12}_{-0.08}$	$8.3^{+0.4}_{-1.4}$	A8	18.8 ± 2.0	-7.32 ± 0.40	6_5–5_4	31.4 ± 9.3	(5, 5, 5, 26, 7, 8, 25)

Note. Column (1): source name. Columns (2)–(5): stellar mass, luminosity, age, and spectral type (SpT). Column (6): disk dust mass (conversion from tabulated 1.3 to 0.9 mm for IRS 48—continuum fluxes in the optically thin approximation, R. H. Hildebrand 1983; the assumptions on temperatures and opacities are as by C. F. Manara et al. 2023 for T Tauri stars; and by L. M. Stapper et al. 2022 for Herbig disks). Column (7): mass accretion rate. Column (8): SO J_N rotational transition. Column (9): SO flux. Column (10): references (ordered by column). Source distances and line transition corrected flux comparisons are available in Appendix E. The stellar parameters of IRS 48 are based on radiative transfer modeling of near-infrared direct imaging and spectroscopy (J. M. Brown et al. 2012; G. Schworer et al. 2017). Its mass accretion rate was estimated form the Pfβ accretion line luminosity by adopting the stellar mass (2.0$M_\odot$) and radius (1.4$R_\odot$) of J. M. Brown et al. (2012). For UY Aur AB, the stellar masses of P. Hartigan & S. J. Kenyon (2003) are consistent within their errors with those reported by F. Long et al. (2019) and C. F. Manara et al. (2019, 2023), who, however, estimated a stellar luminosity of 1.94$L_\odot$, SpT K7, and a much smaller system age of 0.9 $\pm$ 0.4 Myr. For DR Tau, M. Gangi et al. (2022) did not report a stellar age; we thus adopted the estimate of F. Long et al. (2019) from slightly different measurements of the stellar luminosity and effective temperature, still consistent within their uncertainties with those of M. Gangi et al. (2022).

References. (1) G. J. Herczeg et al. (2023), (2) G. J. Herczeg & L. A. Hillenbrand (2014), (3) E. Macías et al. (2021), (4) T. C. Yoshida et al. (2024), (5) M. Vioque et al. (2018), (6) R. O. Gray et al. (2017), (7) L. M. Stapper et al. (2022), (8) S. L. Grant et al. (2022), (9) A. S. Booth et al. (2024a), (10) K. Mooley et al. (2013), (11) C. Wichittanakom et al. (2020), (12) A. Dutrey et al. (2024), (13) G. Schworer et al. (2017), (14) J. M. Brown et al. (2012), (15) S. Ohashi et al. (2020), (16) C. Salyk et al. (2013), (17) A. S. Booth et al. (2024b), (18) A. S. Booth et al. (2023a), (19) P. Hartigan & S. J. Kenyon (2003), (20) C. F. Manara et al. (2023), (21) Y.-W. Tang et al. (2014), (22) M. Gangi et al. (2022), (23) J. Huang et al. (2023), (24) R. Garcia Lopez et al. (2006), (25) this work, and (26) S. L. A. Vieira et al. (2003).

detailed in Appendix D. We note that different assumptions on the excitation temperature do not qualitatively change our results, as the derived flux differences are relatively small. The stellar and disk parameters of interest and the converted SO fluxes are summarized in Table 1 and Appendix D.

With the caveats of a higher detection occurrence toward Herbig stars and our small sample size, we did not detect any correlations between SO luminosity and stellar mass, luminosity, accretion rate, or (sub)millimeter continuum luminosity. However, we identified a tentative anticorrelation between SO luminosity and individual stellar age (see, Appendix E for a more quantitative discussion on the correlations), suggesting that younger systems in our sample have stronger SO emission, perhaps reflecting its intrinsic origin. This tentative trend is qualitatively consistent with the evidence that SO is commonly detected in young embedded protostars. In fact, 76% of the 21 class 0 sources part of the CALYPSO survey (L. Podio et al. 2021), 86% of the class 0 and 57% of the class I sources targeted by the PEACHES survey (T. Artur de la Villarmois et al. 2023), as well as several protostars observed by the eDisk (e.g., C. Flores et al. 2023; M. L. R. van't Hoff et al. 2023; Y. Yamato et al. 2023) and FAUST (e.g., C. Codella et al. 2024; Z. E. Zhang et al. 2024; Y. Oya et al. 2025) ALMA Large Programs show clear evidence of SO emission. Still, in many of these young sources, SO is primarily tracing stellar outflows or disk winds, rather than the disk itself or shocks at the interface between the disk and its surrounding infalling envelope. Moreover, we acknowledge that age estimates of young stellar objects are highly uncertain (D. R. Soderblom et al. 2014), and our sample size is too small to draw a definitive conclusion. In fact, the lack of dependence of the SO flux on the other stellar and disk parameters might simply indicate that multiple SO origins coexist.

4.2. Potential Origins of SO Emission

The production of SO in the gas-phase comes from two groups of processes: (1) (thermal) desorption or sputtering (e.g., T. Aota et al. 2015), and (2) gas-phase SO formation chemistry (e.g., M. L. van Gelder et al. 2021), driven by the production of (2.1) the OH radical, either with endothermic reactions between H_2 and atomic oxygen or by photodissociation of H_2O (e.g., T. W. Hartquist et al. 1980), or (2.2) the SH radical, by desorption of H_2S, which is expected to be the major sulfur carrier in the ices (e.g., T. H. G. Vidal et al. 2017). For both these processes to work, an excess heating or UV source is required, thus explaining why SO is often suggested as a shock tracer. However, this might also explain the higher occurrence of SO toward Herbig stars in our sample as a consequence of their stronger radiation field, especially in the presence of continuum cavities, where direct irradiation of the cavity walls can create favorable conditions, both in terms of

temperature and UV irradiation, for SO desorption or gas-phase formation. We discuss the possible origins of the detected gas-phase SO as follows.

4.2.1. Direct Desorption of SO at the Inner Cavity Edge

The morphology of some sources in our sample, characterized by deep continuum cavities and SO emission arising primarily from or within their rims, suggests that the detected SO could simply be SO vapor sublimated from the icy pebbles trapped at the edge of these cavities. Indeed, detailed modeling has shown that the gas temperature can rise steeply inside continuum cavities, where the gas is exposed to the direct heating and UV irradiation from the host star (e.g., M. Leemker et al. 2022; and M. G. Ubeira Gabellini et al. 2019 in the case of CQ Tau). This "passive" desorption mechanism has been proposed as an explanation for SO emission in IRS 48 (A. S. Booth et al. 2021) and HD 100546 (A. S. Booth et al. 2023a), and may also account for the SO emission morphology of CQ Tau.

However, whether "direct" thermal desorption can be an explanation for SO emission also in other sources is less straightforward. Additionally, this mechanism cannot explain the diversity of SO emission morphologies in our sample. For example, while SO in MWC 758 (Figure 3) and HD 169142 (A. S. Booth et al. 2023b) still arises close to the inner edge of the continuum cavity, it is too patchy to yield robust conclusions on its morphology. In AB Aur, instead, the SO emission peaks slightly beyond, and not inside, the continuum ring (e.g., A. Dutrey et al. 2024; J. Speedie et al. 2025). Finally, for the T Tauri stars in our sample, either they are not known to host continuum cavities (DR Tau and UY Aur), or their SO emission is not colocated with such cavities when present (TW Hya, T. C. Yoshida et al. 2024).

Similar considerations apply to the desorption of other S-bearing volatiles, such as H_2S, that are needed to explain the observed SO emission via gas-phase formation.

4.2.2. Spirals and Companions

Similar to CQ Tau and MWC 758, almost all class II disks with SO detection in our sample show prominent spirals in near-infrared scattered-light images: DR Tau (D. Mesa et al. 2022), AB Aur (J. Hashimoto et al. 2011; A. Boccaletti et al. 2020), UY Aur (Y.-W. Tang et al. 2014), IRS 48 (K. B. Follette et al. 2015), HD 100546 (K. B. Follette et al. 2017), and HD 169142 (possibly triggered by the protoplanet candidate HD 169142 b, I. Hammond et al. 2023). Furthermore, these disks exhibit significantly non-Keplerian gas kinematics (e.g., J. Calcino et al. 2019; S. Casassus et al. 2022; H. Garg et al. 2022; L. Wölfer et al. 2023, 2025; J. Speedie et al. 2024; R. Teague et al. 2025), where spiral-like features have been identified in ^{12}CO observations through residuals in line width, centroid velocity, and brightness temperature. Spirals are also present in the CO line emission of TW Hya (R. Teague et al. 2022), which is otherwise seemingly unperturbed in (sub)millimeter continuum (e.g., S. M. Andrews et al. 2016) and near-infrared imaging (R. van Boekel et al. 2017; but notice that J. H. Debes et al. 2017 identified clear asymmetries moving with non-Keplerian velocity in their scattered-light observations).

This consistent association between disk spirals and SO emission suggests a plausible link between complex gas dynamics and SO chemistry. Indeed, spiral structures in protoplanetary disks are potential drivers of dynamical and chemical activity (e.g., J. D. Ilee et al. 2011): as they propagate through the disk, spirals can compress gas, creating shocks that locally increase temperature and density (T. Ono et al. 2025), favoring the direct thermal desorption of SO, or its gas-phase formation.

While the origin of the spirals detected in CQ Tau and MWC 758 remains uncertain, (sub)stellar companions are promising candidates to explain their origins (e.g., P. Goldreich & S. Tremaine 1979; Z. Zhu et al. 2015). In fact, several companions have been proposed based on their disk morphology or claimed through high-contrast imaging (e.g., R. Dong et al. 2015; M. Reggiani et al. 2018; M. G. Ubeira Gabellini et al. 2019; K. Wagner et al. 2019, 2023; I. Hammond et al. 2022). If these companions were responsible for exciting the spirals by launching Lindblad waves, their Keplerian orbital frequencies should reflect in the spiral motion. However, the current measurements of the spiral motion in these two sources suggest significantly lower angular velocities than those expected from companions inside their cavities (B. Ren et al. 2018; B. S. Safonov et al. 2022), and at the time of writing, no such companions have been confirmed (see, e.g., K. Wagner et al. 2019, 2024; T. Uyama et al. 2020).

As an alternative explanation, these spirals might have been excited by the shadow of a misaligned inner disk (e.g., M. Montesinos et al. 2016; A. Ziampras et al. 2025). In this scenario, the spiral motion would follow the precession of the inner disk rather than the Keplerian velocity at the spiral's radial location (see, e.g., Z. Zhu et al. 2025), thus leaving open the possibility that unseen inner disk companions could indirectly generate the spiral features detected in the outer disk by misaligning the inner disk through gravitational interactions (e.g., S. Facchini et al. 2018; R. Nealon et al. 2018).

Finally, we note that accreting companions themselves could also act as an excess heating source, through either accretion heating (L. I. Cleeves et al. 2015; H. Jiang et al. 2023) or viscous heating around the circumcompanion disks (A. J. Cridland et al. 2025). However, while this process could lead to the desorption and/or gas-phase formation of SO and was proposed to be at the origin of SO emission in HD 100546 and HD 169142 (A. S. Booth et al. 2023a; C. J. Law et al. 2023), its morphology is expected to be potentially more azimuthally localized than what is observed, e.g., in CQ Tau and MWC 758.

All in all, we argue that, by locally heating up a disk, dynamical perturbations, made evident by the presence of spiral-like features in scattered-light observations or gas kinematics, potentially driven by the presence of (yet unseen) companions, could foster the production of gas-phase SO by thermal desorption or gas-phase chemistry. However, we stress that our hypothesis is based on the concurrent presence of SO emission and dynamical perturbations in a small sample with a significant fraction of bright early-type stars, thus making it more difficult to disentangle whether the formation of SO is driven by direct stellar irradiation or excess heating fostered by dynamical perturbations.

4.2.3. Environmental Interactions and Infall

Another possibility is that the observed SO emission is due to environmental interactions, i.e., slow shocks occurring at the interface between the disk and the infalling material (T. Aota et al. 2015; M. L. van Gelder et al. 2021). This interpretation has been proposed to explain the SO emission detected in the class I disks around DG Tau and HL Tau (A. Garufi et al. 2022), IRS 63 (C. Flores et al. 2023), and the class II disks around DR

Tau (J. Huang et al. 2024) and AB Aur (P. Rivière-Marichalar et al. 2020; A. Dutrey et al. 2024; J. Speedie et al. 2025), where prominent gas streamers traced by CO emission on scales of hundreds of astronomical units were detected in Northern Extended Millimeter Array and ALMA observations (see, J. Huang et al. 2023; J. Speedie et al. 2025).

Curiously, both sources with newly reported SO detection introduced in the paper, CQ Tau and MWC 758, are located near the Taurus star-forming region in close proximity to four other disks, HL Tau, DG Tau, DR Tau, and AB Aur, where SO emission was also observed. Interestingly, the Very Large Telescope/SPHERE Guaranteed Time Observation (GTO) and DESTINYS surveys detected signs of ambient material in about a third of the sources in Taurus (A. Garufi et al. 2024), highlighting the importance of environmental interactions in disk evolution as suggested by recent theoretical studies (A. J. Winter et al. 2024; P. Padoan et al. 2025).

While there is no direct evidence for ongoing infall in CQ Tau nor MWC 758, a kilo astronomical unit–scale optical reflection nebulosity was detected by Hubble Space Telescope around CQ Tau (C. A. Grady et al. 2005). In fact, by searching the vicinity of disks hosting large-scale gaseous structures in ALMA data, A. Gupta et al. (2023) found that all such sources have near-infrared and/or optical reflection nebulae in their vicinity, suggesting a strong correlation between large-scale nebulae and late-infall events. This raises the possibility that environmental interactions, although not directly visible in the current kinematic data, may have played a critical role in shaping the chemical and morphological properties of these disks in the past.

We note that companion-, spiral-, and infall-induced SO formations are not mutually exclusive. For instance, the infall of material from the surrounding environment has been proposed as a promising mechanism to generate spirals (e.g., P. Hennebelle et al. 2017; M. Kuffmeier et al. 2019, 2020). In this scenario, the observed spirals could be remnants of past infall events, which can persist on viscous timescales up to $>10^4$ yr in the outer region of disks (J. Calcino et al. 2025). If Bondi–Hoyle accretion onto disks is frequent (A. J. Winter et al. 2024; P. Padoan et al. 2025), disks may never fully evolve in isolation, providing a continuous source of perturbations to sustain SO production.

Meanwhile, infall-driven SO formation can explain the tentative anticorrelation between SO flux and system age. In a word, younger disks with more active dynamical environments, higher infall frequency, and preshock gas density will have stronger detectable SO emission, and the decaying trend of SO could serve as a signal of cloud density dissipation. However, this could well be a consequence of our very small sample sizes and inherent higher occurrence rate toward more massive stars and brighter disks. Indeed, the anticorrelation between SO flux and system age might simply reflect the different origins of SO emission in our sample: infall driven in younger sources and excited by companions or shadows in more evolved systems.

4.3. Implications for Disk Evolution and Planet Formation

The possible link between SO emission and dynamical perturbations underscores the critical role of disk dynamics and environmental interactions in shaping disk chemistry. In this picture, SO serves as a valuable tracer of excess heating induced by spiral density waves, thus providing insights into the mechanisms driving disk evolution and potentially supporting the hypothesis that this process does not take place in isolation.

The presence of potentially frequent dynamical perturbations raises two concerns. On the one hand, these disks may not always reach (quasi-)equilibrium chemistry, since the relatively long chemical timescales can be comparable to or even longer than the local dynamical timescale (D. Semenov & D. Wiebe 2011; K. I. Öberg et al. 2023). On the other hand, these perturbations lead to significant azimuthal asymmetries, which will change the local material and energy sources for chemical reactions. Both could have major implications for the interpretation of the disk chemistry, as most works assume a static disk over the simulation time and set up the thermo-chemical model as azimuthally symmetric. For example, the CS/SO ratio may not be a robust indicator of the C/O ratio when CS and SO are forward modeled with static and passively irradiated disk models (e.g., R. Le Gal et al. 2019; L. Keyte et al. 2023; J. Huang et al. 2024).

If confirmed, this link between SO formation and dynamical perturbations might have profound implications for planet formation. First, it shows that dynamical perturbations can significantly influence the distribution of volatiles, challenging the traditional view that planets inherit their composition solely from unperturbed disks (e.g., K. I. Öberg et al. 2011; C. Eistrup et al. 2016). In addition, the presence of SO near the rims of continuum disk cavities highlights these regions as chemically active zones, potentially influencing the composition of proto-planets forming within the rings (e.g., N. van der Marel et al. 2021b; L. Rampinelli et al. 2024). Future observations mapping the chemical inventory of CQ Tau and MWC 758, such as those performed for IRS 48 and HD 100546 (A. S. Booth et al. 2024a, 2024b), will be crucial to assess the relationship between SO chemistry and dynamical perturbations and to better under-stand the composition of the planet-forming material.

5. Summary and Conclusions

We report the serendipitous detection of the SO $J_N = 6_5$–5_4 rotational line transition in archival ALMA observations of the planet-forming disks around CQ Tau and MWC 758, two dynamically perturbed systems known for their prominent spiral structures in scattered-light observations. SO emission is detected with 4.9σ significance in CQ Tau and 3.4σ significance in MWC 758. In both cases, it arises preferentially from the edge of the continuum cavity; but while in CQ Tau, it comes in the shape of a ring and is qualitatively compatible with Keplerian rotation; the SO emission is more extended, with a less clear morphology and kinematics in MWC 758.

These results add to the growing sample of SO-bearing class II disks, which now includes nine systems, six of which are Herbig stars with large inner cavities. We argue that the detection of SO in these dynamically perturbed disks suggests a possible link between disk dynamical perturbations and sulfur chemistry. In this picture, strong additional heating and/or turbulence-driven dust collisions, whether caused by yet unseen massive companions, spirals (due to companions themselves or shadows), or infall, can foster the thermal desorption of SO or its production in the gas-phase. However, we stress that, since our sample is small and made up by a significant fraction of bright and massive Herbig stars, "direct" thermal desorption due to passive stellar irradiation remains a possible explanation for the origin of SO emission in at least some of these systems.

We found no statistically significant correlations between SO flux and stellar or disk parameters other than a tentative anticorrelation between SO flux and system age, suggesting that

younger disks, with more active dynamical environments, are likely to have either stronger SO emission or different origins for SO emission. This could be infall driven in younger sources and due to "passive" irradiation or "active" spiral-driven thermal desorption/dust shattering in older perturbed systems.

The detection of SO in such dynamically active systems raises the possibility that chemical evolution might take place on significantly shorter timescales than those commonly assumed in disk evolution and planet formation models. Our results have important implications for interpreting disk chemistry and predicting the composition of forming planets, since tracers such as the CS/SO ratio might not be reliably used to infer the C/O ratio in dynamically perturbed and chemically active disks if forward models are not representative of the out-of-equilibrium environment conditions, and emphasize the need for future studies to consider chemical and dynamical evolution simultaneously.

Future higher resolution and sensitivity observations will be crucial to unravel the detailed mechanisms linking disk dynamics, chemistry, and planet formation in these systems. In particular, a larger sample of SO-bearing disks, combined with detailed kinematic studies on both large and small scales, will help to clarify the role of environmental interactions and dynamical perturbations in shaping disk chemistry.

Appendix A
Data

We introduce the archival observations underlying our analysis. Key information is summarized in Table 2.

CQ Tau. The observations were conducted in Cycles 2, 4, and 5 between 2015 August and 2017 November, as part of the programs 2013.1.00498.S (PI: L. Pérez), 2016.A.00026.S (PI: L. Testi), and 2017.1.01404.S (PI: L. Testi). These programs used only Band 6 receivers, and the data were correlated from eight spectral windows (SPWs) in dual polarization mode. Six SPWs were set in frequency division mode (FDM), one with 1920 channels 244.1 kHz wide centered at 230.7 GHz, two with 960 channels 448.3 kHz wide centered at 219.7 and 220.2 GHz, two with 60 channels 7.8 MHz wide centered at 218.8 and 219.3 GHz, one with 120 channels 3.9 MHz wide centered at 231.2 GHz, all spanning a total bandwidth of 468.8 MHz. The remaining two SPWs, centered at 217.0 (2013.1.00498.S), 217.6 (2016.A.00026.S and 2017.1.01404.S), and 232.4 GHz, were set in time division mode (TDM), with 128 channels 15.6 MHz wide, and spanned a total bandwidth of 2.0 GHz.

For the program 2013.1.00498.S, the observations used an array with baseline lengths from 15.1 m to 1.5 km (resolution of $\approx 0\rlap{.}''260$) and 35 antennas in the C34-7 configuration. The total integration time on the science target was ≈ 15 minutes. The bandpass calibrator J0423-0120 and the flux calibrator J0510+1800 were observed at the beginning of the observing block; the phase calibrator J0550+2326 and an additional delay calibrator J0547+2721 were observed in an alternating sequence with the science target, every ≈ 10 and 15 minutes.

For the program 2016.A.00026.S, the observations used an array with baseline lengths from 81.0 m to 3.7 km (resolution of $\approx 0\rlap{.}''110$) and 41 antennas in the C40-7 configuration. The total integration time on the science target was ≈ 20 minutes. The bandpass and flux calibrator J0510+1800 was observed at the beginning of the observing block; the phase calibrator J0547+2721 was observed in an alternating sequence with the science target, every ≈ 1–2 minutes. An additional "check" calibrator, J0521+2112, was observed every ≈ 7 minutes to assess the quality of the phase transfer.

For the program 2017.1.01404.S, the observations used an array with baseline lengths from 92.1 m to 8.5 km (resolution of $\approx 0\rlap{.}''060$). Two execution blocks (EBs) were scheduled, with 44 and 48 antennas, respectively, in the C43-8 configuration. The total integration time on the science target was ≈ 30 minutes for each EB. The bandpass, flux, and "check" calibrator J0510+1800 was observed at the beginning of the observing block, then every ≈ 10 minutes to assess the quality of the phase transfer, the phase calibrator J0521+2112 was observed in an alternating sequence with the science target, every ≈ 1–2 minutes.

Table 2
Summary of the Archival ALMA Observations Analyzed in This Paper

Source	Project Code	PI	Obs. Date (dd/mm/yy)	ToS (min)	MBL (km)	No. of Ant.	Phase Cal.	Flux Cal.	PWV (mm)	MRS (arcsec)
(1)	(2)	(3)	(4)	(5)	(6)	(7)	(8)	(9)	(10)	(11)
CQ Tau	2013.1.00498.S	Pérez	30/08/15	15.817	1.5	35	J0550+2326	J0510+1800	1.18	2.9
	2016.A.00026.S	Testi	07/08/17	19.656	3.7	41	J0547+2721	J0510+1800	0.93	1.3
	2017.1.01404.S	Testi	20/11/17	29.083	8.5	44	J0521+2112	J0510+1800	0.53	0.8
			23/11/17	29.050	8.5	48			0.46	1.0
...	...	...	10/10/17	44.633	16.2	47	...	...	0.40	0.3
...	...	...	10/10/17	44.617	16.2	47	...	...	0.41	0.3
...	...	...	11/10/17	44.600	16.2	47	...	...	1.31	0.3
...	...	...	15/10/17	44.667	16.2	52	...	...	2.45	0.4
MWC 758	2017.1.00940.S	Ricci	16/10/17	44.717	16.2	52	J0521+2112	J0510+1800	2.74	0.4
...	...	...	09/10/17	38.500	3.1	44	...	...	2.24	1.6
...	...	...	17/10/17	38.517	2.5	45	...	...	2.18	2.4
...	...	...	27/10/17	38.550	2.5	46	...	...	2.38	2.3
...	...	...	28/10/17	38.517	2.5	45	...	...	1.04	2.5

Note. Column (1): source. Column (2): project code. Column (3): principal investigator (PI). Column (4): observation date. Column (5): integration time on the science target (time on source, ToS). Column (6): maximum baseline length (MBL). Column (7): number of antennas. Columns (8) and (9): phase and flux calibrators. Column 10: precipitable water vapor (PWV). Column (11): maximum recoverable scale (MRS).

MWC 758. The observations were conducted in Cycle 5 between 2017 October and December as part of the program 2017.1.00940.S (PI: L. Ricci). The data were correlated from four SPWs in dual polarization mode. Two SPWs were set in FDM each with 1920 channels 976.6 kHz wide centered at 219.5 and 231.5 GHz and spanning a total bandwidth of 1.9 GHz. The remaining SPWs, centered at 217.5 and 234.2 GHz, were set in TDM, with 128 channels 15.6 MHz wide, and spanning a total bandwidth of 2.0 GHz. The target was observed in the more compact C43-6 configuration (short baselines, four scheduled EBs), and the more extended C43-10 configuration (long baselines, five scheduled EBs).

The observations at short baselines used an array with baseline lengths from 15.1 m to 2.5 or 3.1 km (resolution of $\approx 0\rlap{.}''130$) and between 44 and 46 antennas. The total integration time on the science target was ≈ 40 minutes for each EB. The bandpass and flux calibrator J0510+1800 was observed at the beginning of each EB, while the phase calibrator J0521+2112 was observed in an alternating sequence with the science target, every ≈ 10 minutes. An additional "check" calibrator, J0519+2744, was observed every ≈ 30 minutes to assess the quality of the phase transfer.

The observations at long baselines used an array with baseline lengths from 41.4 or 233.0 m to 16.2 km (resolution of $\approx 0\rlap{.}''020$) and between 47 and 52 antennas. Five EBs were scheduled. The total integration time on the science target was ≈ 45 minutes for each of them. The bandpass and flux calibrator J0510+1800 was observed at the beginning of each EB, while the phase calibrator J0521+2112 was observed in an alternating sequence with the science target, every ≈ 1–2 minutes. An additional "check" calibrator, J0518+2054, was observed every ≈ 15 minutes to assess the quality of the phase transfer.

Appendix B
Self-calibration

To begin with, we created pseudocontinuum data sets flagging channels within $\pm 15\,\mathrm{km\,s^{-1}}$ of the systematic velocity around the rest frequencies of the ^{12}CO ($J = 2$–1 at 230.5380 GHz), ^{13}CO ($J = 2$–1 at 220.3986 GHz), C^{18}O ($J = 2$–1 at 219.5603 GHz),

DCN ($J = 3$–2 at 217.2385 GHz), SO ($J_N = 6_5$–5_4 at 219.9494 GHz), and H$_2$CO ($N_{K_a,K_c} = 3_{0,3}$–$2_{0,2}$, $3_{2,1}$–$2_{2,0}$, $3_{2,2}$–$2_{2,1}$, and $9_{1,8}$–$9_{1,9}$ at 218.2221, 218.7601, 218.4756, and 216.5686 GHz) transitions.

These pseudocontinuum EBs were channel averaged ensuring a $<1\%$ reduction in peak response to a point source at the edge of the primary beam to avoid bandwidth smearing, according to the criterion of A. H. Bridle & F. R. Schwab (1999), and imaged (separately) over the entire primary beam, using the task tclean. CLEANing was performed over a user-defined elliptical mask of $0\rlap{.}''85 \times 0\rlap{.}''72$, position angle (PA) $= 55°$ for CQ Tau and $0\rlap{.}''80 \times 0\rlap{.}''80$, PA $= 62°$ for MWC 758 that covers all the continuum emission, with a threshold of $\approx 6\sigma$, where σ is the rms noise calculated over an emission-free annular region between $4''$ and $6''$ centered on the source phase center and larger than the continuum emission extent, and ≈ 8 pixels along the synthesized beam minor axis. We adopted the multiscale deconvolver (T. J. Cornwell 2008), with scales including a point source and some (sub)multiples of the synthesized beam that could be accommodated within the user-defined mask ([0, 2, 4, 8, 12] for short baseline and [0, 2, 4, 8, 16, 24] for long-baseline observations), with a preference for smaller ones (smallscalebias=0.6), cycleniter=300, gain=0.3, and a briggs weighting scheme with robust=0.5 (D. S. Briggs 1995). For CQ Tau, since some of the data were taken in early ALMA cycles, we recomputed the weights using the task statwt combining different polarizations, scans, and SPWs.

Subsequently, a round of phase-only self-calibration was performed on each EB (separately) to increase their SNR prior to alignment. The gain solutions were computed using the task gaincal over an infinite solution interval, for both polarizations together, combining all the available SPWs and time scans, and rejecting those gain solutions corresponding to antennas with <3 baselines and SNR < 4. We then shifted the phase centers of these self-calibrated EBs to a common direction, chosen to be that of the phase center of the long-baseline EB with the highest peak SNR. The alignment was performed in visibility space, minimizing the phase differences between EBs in the widest continuum SPW, and

checked for by comparing the ratio images (reconstructed using the same parameters described above) of each data set to the reference EB (see S. Casassus & M. Cárcamo 2022; R. A. Loomis et al. 2025). While in the case of CQ Tau the peak SNR of each self-calibrated EB was high enough ($\gtrsim$65) to provide a significant reduction of the amount of structures in the ratio images, indicative of an accurate alignment, for MWC 758, the much lower peak SNR, especially for the long-baseline EBs ($\lesssim$15), often led to a (marginal) worsening of the EB alignment. Thus, since the direct inspection of the images suggested that the EBs were already almost perfectly aligned, for MWC 758, we chose not to shift the EBs.

For both sources, we inspected the EBs for amplitude-scale offsets, plotting the ratio of their projected visibilities to those of a reference EB. For CQ Tau, the EB with highest peak SNR shows flux offsets >30% compared to the others. Thus, we adopted as a reference EB the one taken on 2017 November 23, because of its lower phase rms (22°.58) and higher peak SNR compared to the remaining ones. Instead, for MWC 758, we selected as a reference EB the one taken on 2017 December 28, because its peak SNR is the highest among the available EBs, and its phase rms (16°.72) is lower than for the other SBs. For both sources, most EBs show a (sometimes significant) dependence of the visibility amplitude ratio on the deprojected baselines, which we interpreted as an indication of phase-decoherence. For this reason, although for some EBs flux-scale offsets >4% were estimated, at this stage, we chose not to rescale their amplitudes. Instead, we performed a first iteration of phase-only self-calibration, first on the concatenated short-baseline observations and then combining short- and long-baseline data to correct for decoherence and identify more accurate flux-scale offsets.

Self-calibration was performed iteratively, first on the short-baseline observations and then on the combined short- and long-baseline EBs (e.g., S. M. Andrews et al. 2018). The images were reconstructed after each step adopting the same fiducial parameters described above, except for the long-baseline observations of MWC 758, whose best trade-off between angular resolution and peak SNR was obtained for `robust=1.0`. For the short-baseline data, the gain solutions were first computed separately for each polarization on an infinite solution interval, combining different SPWs and time scans. Then, the gain solutions were computed on progressively shorter solution intervals of 360, 120, 60, and 20 s, for both polarizations together, combining different SPWs and time scans (but no scans were combined for solution intervals shorter than the average scan length). The gain solutions for antennas with < 4 baselines and SNR < 3 were flagged. Visual inspection led to further manual flagging of too large phase-gain solutions. For the long-baseline data, we followed a similar procedure, with solution intervals decreasing from the full EB, to 360, 120, 60, 30, and 18 s,[24] rejecting gain solutions corresponding to antennas with < 4 baselines and SNR < 2 (for CQ Tau) or 3 (for MWC 758). For CQ Tau, the peak SNR increased from 112.77 to 151.32 ($\approx$34%) after self-calibration of the short-baseline data and from 138.88 to 181.98 ($\approx$31%) after self-calibration of the combined short- and long-baseline EBs. For MWC 758, the peak SNR increased from 317.43 to 442.55 ($\approx$39%) after self-calibration of the short-baseline

observations and from 171.13 to 186.57 ($\approx$9%) after self-calibration of the combined short- and long-baseline EBs.

We reinspected the amplitude ratios between different EBs and the reference ones after each self-calibration step, finding that the flux offsets were progressively reduced, and decoherence decreased in most cases. Then, we rescaled those EBs that showed flux ratios >4% and performed a new self-calibration iteration. For CQ Tau, the peak SNR increased from 148.65 to 201.44 ($\approx$36%) after self-calibration of the short-baseline data and from 164.87 to 222.13 ($\approx$35%) after self-calibration of the combined short- and long-baseline EBs. For MWC 758, the peak SNR increased from 322.03 to 450.81 ($\approx$40%) after self-calibration of the short-baseline observations and from 167.33 to 176.44 ($\approx$5%) after self-calibration of the combined short- and long-baseline EBs.

We then performed two cycles of amplitude and phase self-calibration. The solutions were obtained with an infinite solution interval, first combining all the available SPWs and scans, then combining only the SPWs, for both polarizations together. Images were reconstructed with the same fiducial parameters described above and a CLEANing threshold of $\approx$1σ. In all cases, gain solutions for antennas with < 4 baselines and SNR < 5 were flagged. Amplitude gains >20% were also flagged, and phase-gain solutions were further visually inspected and manually flagged when too large. For CQ Tau, both steps were successful and led to an improvement in the peak SNR from 222.35 to 224.17 ($\lesssim$1%), while for MWC 758 the peak SNR improved from 167.98 to 179.98 ($\approx$7%) after the first step, and no second iteration was performed.[25]

Finally, we applied the phase shifts, flux scaling, and gain solutions to the original data sets (i.e., those including the previously flagged line emission channels) and time-binned the self-calibrated measurement sets by 30 s to reduce the data volume. Then, using the CASA `v6.2.1-7` implementation of the `uvcontsub` task, with `solint=1`, `fitorder=1`, and excluding the same channels used to create the pseudocontinuum data sets, these measurement sets were continuum subtracted, and independent data sets for each relevant rotational transition were created.

The calibration and imaging scripts are available on GitHub.[26]

Appendix C
Imaging and Summary Plots

The continuum images were reconstructed from the measurement sets obtained after the last step of phase and amplitude self-calibration, time averaged by 30 s. These (line-flagged) data sets were CLEANed with the same fiducial parameters described in Appendix B, `robust=0.0` for CQ Tau and `robust=1.0` for MWC 758, a noise threshold of $\approx$1σ (the rms was measured on an emission-free circular annulus between 4″ and 6″ centered on the source phase center using the task `imstat`), and `gain=0.02` (to minimize any artifacts in the continuum cavities). Our fiducial images are displayed in Figure 1, while Table 3 summarizes their imaging parameters and continuum properties.

As is commented on in Section 3, the continuum emission from both sources shows significant evidence of ongoing dynamical

---

[24] For MWC 758, we only considered `solint` parameters $\geqslant$60 s. For shorter solution intervals, the peak SNR leveled off, and the phase-gain solutions obtained for the EBs taken on 2017 December 15 and 16 became very extreme (> 150° or <−150°) and heavily time-dependent for most antennas, leading to substantial flux-scale offset variations among the long-baseline EBs.

[25] Because the too short solution intervals (scan length $\approx$30–60 s) led to too high gain solutions for most of the antennas.
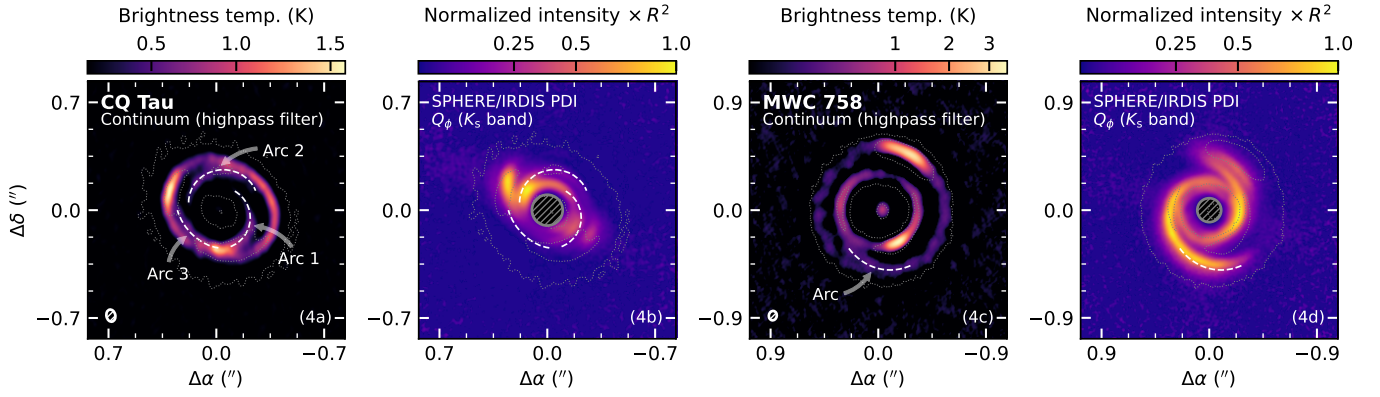[26] https://github.com/fzagaria/selfcal_CQTau_and_MWC758

Figure 4. Highpass-filtered 1.3 mm continuum emission (panels (4a), (4c)), and polarized intensity (panels (4b), (4d)), for CQ Tau and MWC 758. The dotted gray lines display the $[5, 65] \times \sigma$ (CQ Tau) and the $[5, 40] \times \sigma$ (MWC 758) emission contours. The synthesized CLEAN beam is shown as an ellipse in the bottom left corner of each continuum panel. The regions within 0″1 of the scattered-light images cannot be accessed because of the coronagraph and are masked out.

Table 3
Continuum Emission Imaging Parameters and Key Properties

| Source | Wav. | Rob. | Beam Size | PA | rms Noise | Peak Intensity | Peak SNR | Integrated Flux |
| | (mm) | | (″²) | (deg) | (mJy beam⁻¹) | (mJy beam⁻¹) | | (mJy) |
(1)	(2)	(3)	(4)	(5)	(6)	(7)	(8)	(9)
CQ Tau	1.33	0.0	0.055×0.039	−4.1	1.43×10^{-3}	1.29	90.04	146.80 ± 0.37
MWC 758	1.33	1.0	0.066×0.044	8.5	6.46×10^{-3}	1.11	172.33	58.01 ± 0.30

Note. Column (1): source. Column (2): average observation wavelength (wav.). Column (3): Briggs weighting `robust` parameter (rob.). Columns (4) and (5): synthesized beam size and PA. Column (6): rms noise. Column (7): peak intensity. Column (8): peak SNR. Column (9): integrated flux. Uncertainties were estimated as the standard deviation of the integrated fluxes measured in 24 off-source nonoverlapping copies of the mask used to image the continuum over.

perturbations in the form of high-contrast asymmetries. Such asymmetries show up more distinctly in panels (a) and (c) of Figure 4, which display the highpass-filtered continuum emission from both sources. These highpass-filtered maps were obtained by subtracting to the images reconstructed with `robust=0.5` and `1.5` their convolution with Gaussian kernels with a standard deviation of 5 and 8 pixels, respectively. In the case of MWC 758, R. Dong et al. (2018) had already reported the presence of an azimuthally wide arc, colocated with one of the scattered-light spirals (see panel (4d), which shows the K_s-band Q_ϕ polarized differential image published by B. B. Ren et al. 2023), that connects the cavity rim with a bright annular structure. For CQ Tau, the higher SNR and angular resolution of our combined data set allowed detecting, for the first time, three arcs veering from the continuum ring toward the central cavity. One of them (labeled "Arc 1" in panel (4a)) is connected with one of the spirals detected in scattered-light (see panel (4b), which also shows the K_s-band Q_ϕ polarized differential image published by B. B. Ren et al. 2023), suggesting that they might be tracing the same physical disk structure.

For SO, the continuum-subtracted measurement sets were imaged using `tclean` with `specmode='cube'`, 23 channels of 0.7 km s⁻¹ (corresponding to absolute velocities from −1.3 to 13.9 km s⁻¹ in the LSRK reference frame) for CQ Tau and 7 channels of 1.4 km s⁻¹ (corresponding to absolute velocities from 1.7 to 10.1 km s⁻¹ in the LSRK reference frame) for MWC 758 (plum area in the spectra in Figure 2), a `multiscale` deconvolver, and scales including a point source and submultiples of the synthesized beam (i.e., [0, 2, 4, 8]). CLEANing was performed with a common restoring beam across different channels, ≈8 pixels along the synthesized beam minor axis, a

Table 4
Deprojection and Stacking Parameters (Adopted from A. F. Izquierdo et al. 2025)

| Source | i | PA | $M_\star$ | d | v_{sys} |
| | (deg) | (deg) | $(M_\odot)$ | (pc) | (km s⁻¹) |
(1)	(2)	(3)	(4)	(5)	(6)
CQ Tau	−36.3	235.1	1.40	149.4	6.19
MWC 758	19.4	240.3	1.40	155.9	5.89

Note. Column (1): source. Column (2): inclination. Column (3): position angle. Column (4): stellar mass. Column (5): distance. Column (6): systematic velocity. The fiducial stellar masses adopted in our analysis were inferred dynamically by modeling CO emission (A. F. Izquierdo et al. 2025) and are consistent, within the uncertainties, with the spectroscopically based estimates reported in Section 2.1 and Table 1. We prefer such dynamical estimates because they are not affected by the systematics in the pre-main-sequence evolutionary tracks (see, R. Garcia Lopez et al. 2006; M. Vioque et al. 2018) and for consistency with exoALMA.

1σ threshold (the rms was estimated as for the continuum), and a conservative `gain=0.01`, over a user-defined mask, either the same one used for the continuum (equally across all the channels) or a Keplerian mask (generated using the code of R. Teague 2020; and the geometric parameters of P. Curone et al. 2025; and A. F. Izquierdo et al. 2025; listed in Table 4). For MWC 758, some differences between the images reconstructed with the continuum and Keplerian masks can be seen due to clear non-Keplerian emission features (see, e.g., teardrop plot in Figure 2). Different weighting schemes, `robust` parameters, and Gaussian uv-tapers were tested.
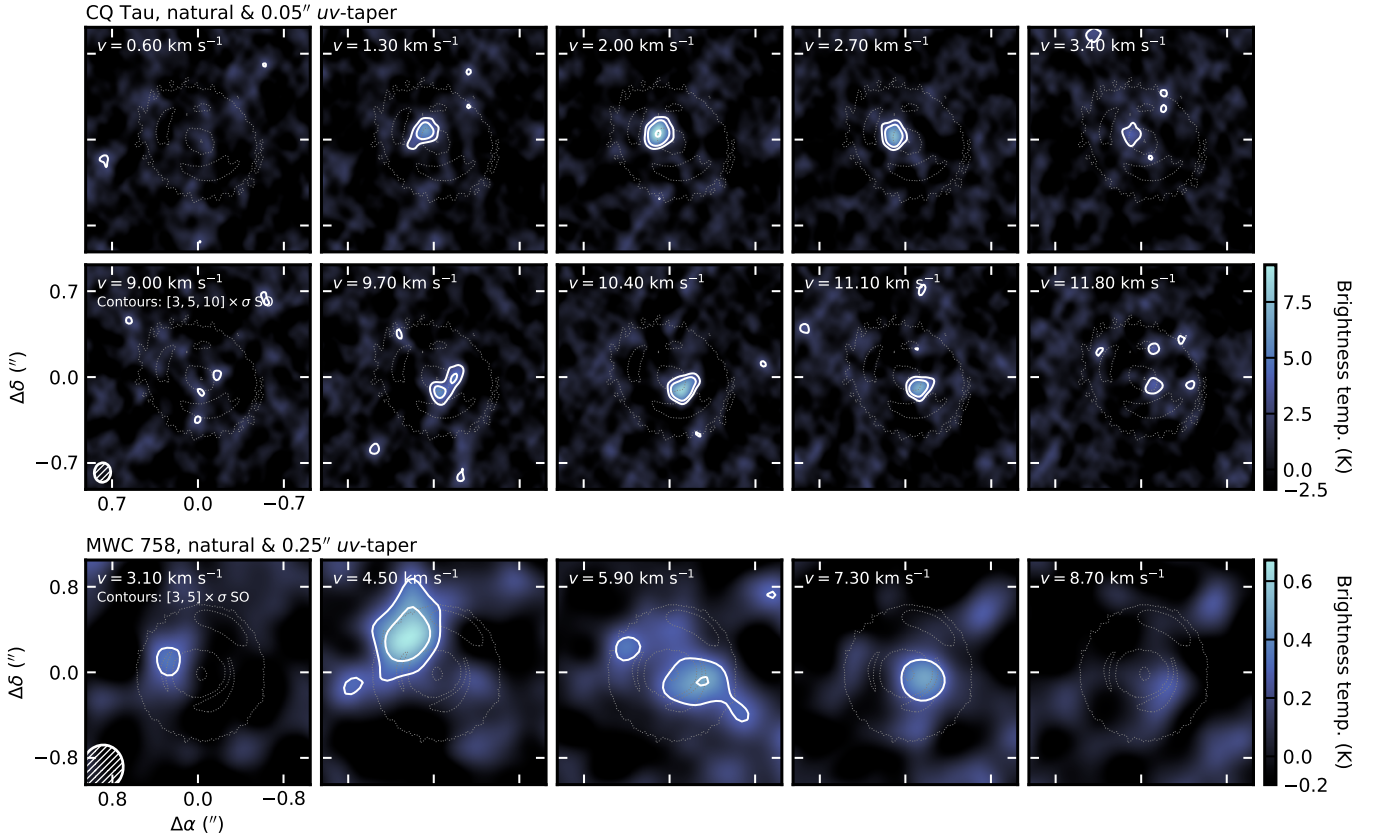
Figure 5. SO channel maps for CQ Tau ($v_{sys} = 6.2$ km s^{-1}, top rows) and MWC 758 ($v_{sys} = 5.9$ km s^{-1}, bottom row). The dotted gray contours display the $[5, 65] \times \sigma$ (CQ Tau) and the $[5, 40] \times \sigma$ (MWC 758) continuum emission levels. The synthesized CLEAN beam is shown as an ellipse in the bottom left corner of the bottom left panels.

Table 5
SO Emission Imaging Parameters and Key Properties

Source	Weighting	uv-tapering ($''$)	Beam Size ($''^2$)	PA (deg)	Avg. rms Noise (mJy beam^{-1})	Peak Intensity (mJy beam^{-1})	Peak SNR
(1)	(2)	(3)	(4)	(5)	(6)	(7)	(8)
CQ Tau	natural	0.05	0.159×0.133	-6.76	7.44×10^{-1}	7.67	10.31
MWC 758	natural	0.25	0.428×0.326	-11.73	6.61×10^{-1}	4.39	6.65

Note. Column (1): source. Column (2): weighting. Column (3): uv-tapering. Columns (4) and (5): synthesized beam size and PA. Column (6): average rms noise across the line-emission channels. Column (7): peak intensity. Column (8): peak SNR.

Our fiducial images were reconstructed with `natural` weighting scheme and a Gaussian uv-taper with $0''.05$ (CQ Tau) and $0''.25$ (MWC 758) full width at half-maximum. Some relevant channel maps are displayed in Figure 5, and their imaging parameters and emission properties are summarized in Table 5. These same fiducial images were also used to generate the integrated intensity, peak intensity, and velocity maps displayed in Figure 3, using `bettermoments`,[27] a Python package that collapses (smoothed and spatially or spectrally masked) image cubes along the velocity axis to generate moment maps (R. Teague & D. Foreman-Mackey 2018). Because of the moderate detection significance of SO, we did not apply any channel or noise clipping. No clear signs of spacial noise correlations can be seen in any of the moment maps, nor in any channel map, for all weighting schemes.

To assess the SO detection significance, a set of images were reconstructed with these same fiducial parameters, but across a much wider velocity range ($\gtrsim 200$ km s^{-1}), essential to accurately determine the background noise in line free channels. We used `gofish`[28] (R. Teague 2019), a Python package that extracts and averages spectra from an image cube across a given disk region and, under the assumption of a Keplerian velocity field, corrects for the known disk rotation by shifting such spectra to a common line center (see, H.-W. Yen et al. 2016), to stack our SO emission lines and increase their peak SNR, adopting the physical and geometrical parameters in Table 4. Such an improvement can be seen by comparing the gray and blue spectra in the insert in panels (a) and (c) of Figure 2.

---

[27] https://bettermoments.readthedocs.io/en/latest/index.html

[28] https://fishing.readthedocs.io/en/latest/index.html

Appendix D
Flux Conversion between SO Transitions

To fairly compare the SO emission detected in different transitions, we estimated the SO $J_N = 6_5–5_4$ flux for disks that do not have SO $J_N = 6_5–5_4$ observations, based on the line flux from the detected transition. We considered two regimes: optically thin and optically thick. This estimation depends on the excitation conditions, energy levels, and line properties. Our conversion results are summarized in Table 6.

In the optically thin regime, assuming local thermodynamic equilibrium and a constant excitation temperature ($T = 30$, 50, and 70 K), we calculated the flux ratio of the known line F_1 to the desired line flux F_2 by (P. F. Goldsmith & W. D. Langer 1999)

$$\frac{F_2}{F_1} = \frac{\nu_2}{\nu_1} \cdot \frac{A_{ul}^{(2)} g_u^{(2)} e^{-E_u^{(2)}/kT}}{A_{ul}^{(1)} g_u^{(1)} e^{-E_u^{(1)}/kT}}, \tag{D1}$$

where k is the Boltzmann constant, ν_1, ν_2 are the line frequencies, $A_{ul}^{(1)}$, $A_{ul}^{(2)}$ are the Einstein A_{ul} coefficients, $g_u^{(1)}$, $g_u^{(2)}$ are the statistical weights of the upper levels, and $E_u^{(1)}$, $E_u^{(2)}$ are the upper level energies of the two transitions.

In the optically thick case, the line becomes saturated, and the intensity depends primarily on the excitation temperature and source size, $F \propto B_\nu(T) \cdot \Omega$, where $B_\nu(T)$ is the Planck function at the excitation temperature T and frequency ν, and Ω is the solid angle of the emitting region. Assuming the same excitation temperature and emitting area for both transitions, we have

$$\frac{F_2}{F_1} \approx \frac{B_{\nu_2}(T)}{B_{\nu_1}(T)} \approx \frac{\nu_2^2}{\nu_1^2} \tag{D2}$$

where the last step follows from the Rayleigh–Jeans approximation.

Table 6
SO Flux Conversion

Source	d (pc)	SO Transition	F_{SO} Obsv. (mJy km s^{-1})	Optical Depth	T (K)	F_{SO} at 140 pc (mJy km s^{-1})
(1)	(2)	(3)	(4)	(5)	(6)	(7)
⋯	⋯	$7_8–6_7$	13 ± 3	⋯	⋯	2.4
⋯	⋯	$6_5–5_4$	⋯	Thin	30	1.7
TW Hya	60.1 ± 0.1	$6_5–5_4$	⋯	Thin	50	0.9
⋯	⋯	$6_5–5_4$	⋯	Thin	70	0.7
⋯	⋯	$6_5–5_4$	⋯	Thick	⋯	1.0
⋯	⋯	$7_8–6_7$	343 ± 26	⋯	⋯	204.6
⋯	⋯	$6_5–5_4$	⋯	Thin	30	143.0
HD 100546	108.1 ± 0.4	$6_5–5_4$	⋯	Thin	50	77.2
⋯	⋯	$6_5–5_4$	⋯	Thin	70	59.3
⋯	⋯	$6_5–5_4$	⋯	Thick	⋯	85.3
AB Aur	155.9 ± 0.9	$6_5–5_4$	330 ± 10	⋯	⋯	409.4
⋯	⋯	$7_8–6_7$	1063 ± 23	⋯	⋯	1007.9
⋯	⋯	$6_5–5_4$	⋯	Thin	30	704.4
IRS 48	136.3 ± 1.9	$6_5–5_4$	⋯	Thin	50	380.5
⋯	⋯	$6_5–5_4$	⋯	Thin	70	292.2
⋯	⋯	$6_5–5_4$	⋯	Thick	⋯	420.0
⋯	⋯	$8_8–7_7$	120 ± 10	⋯	⋯	80.8
⋯	⋯	$6_5–5_4$	⋯	Thin	30	58.5
HD 169142	114.9 ± 0.3	$6_5–5_4$	⋯	Thin	50	29.0
⋯	⋯	$6_5–5_4$	⋯	Thin	70	21.5
⋯	⋯	$6_5–5_4$	⋯	Thick	⋯	33.0
UY Aur AB	152.3 ± 0.9	$6_5–5_4$	N/A	⋯	⋯	N/A
DR Tau	193.0 ± 1.2	$6_5–5_4$	195 ± 9	⋯	⋯	370.5
CQ Tau	149.4 ± 1.3	$6_5–5_4$	72.4 ± 14.6	⋯	⋯	82.4
MWC 758	155.9 ± 0.8	$6_5–5_4$	31.4 ± 9.3	⋯	⋯	38.9

Note. Column (1): source name. Column (2): source distance. Column (3): SO J_N transition. Upper state energies are 35.0, 81.2, and 87.5 K for the $J_N = 6_5–5_4$, $7_8–6_7$, and $8_8–7_7$ transitions, respectively; see the Leiden Atomic and Molecular Database (https://home.strw.leidenuniv.nl/~moldata/SO.html), and W. W. Clark & F. C. De Lucia (1976). Column (4): SO flux. Column (5): optical depth assumption. Column (6): excitation temperature assumption. Column (7): SO $J_N = 6_5–5_4$ flux rescaled to 140 pc.

Appendix E
Correlation Test

We visualize the stellar and disk parameters of interest and the converted SO fluxes summarized from Tables 1 and 6 in the pair plot in Figure 6. We adopted the Pearson correlation coefficient (PCC) and the corresponding p-values to quantitatively assess how the SO fluxes correlate with other parameters, which are labeled in the pair plots. While no statistically significant ($p < 0.05$) correlations are found with stellar mass, luminosity, accretion rate, and disk mass, the SO fluxes show a tentative anticorrelation with system age, with a PCC of -0.82 when SO flux is in logarithmic space, and age is in linear space.
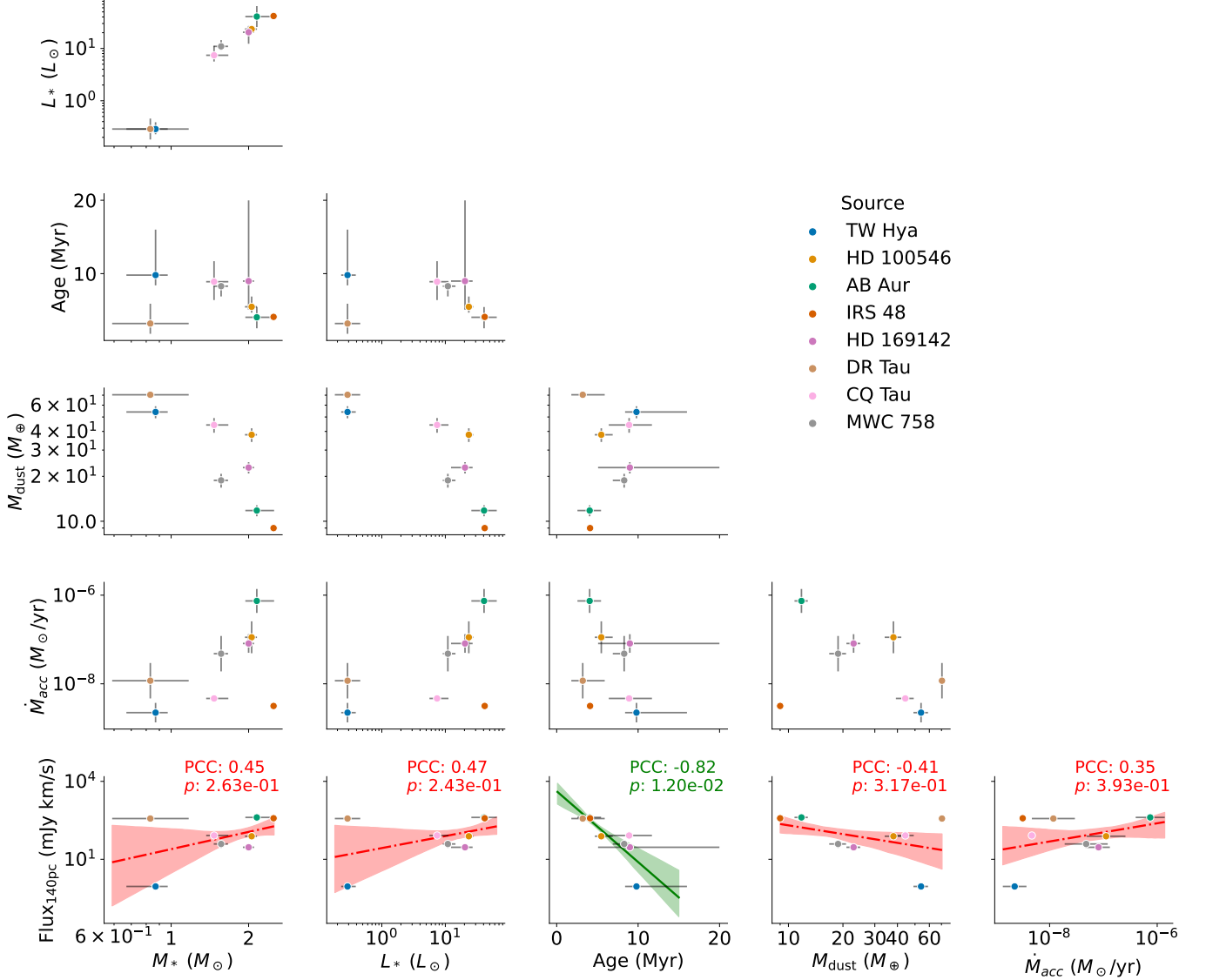
Figure 6. Pair plot of stellar and disk parameters for all known SO-bearing class II protoplanetary disks. The bottom row lists the calculated PCC and the corresponding p-values between the scaled SO flux and other parameters. A linear regression analysis is performed for each parameter pair, with the best fits shown as solid lines and the 16th and 84th percentiles of the bootstrap distribution shown as collar dashes, indicating 1σ confidence interval. The linear regression is shown in green when $p < 0.05$.

ORCID iDs

Francesco Zagaria ● https://orcid.org/0000-0001-6417-7380
Haochang Jiang ● https://orcid.org/0000-0003-2948-5614
Gianni Cataldi ● https://orcid.org/0000-0002-2700-9676
Stefano Facchini ● https://orcid.org/0000-0003-4689-2684
Myriam Benisty ● https://orcid.org/0000-0002-7695-7605
Yuri Aikawa ● https://orcid.org/0000-0003-3283-6884
Sean Andrews ● https://orcid.org/0000-0003-2253-2270
Jaehan Bae ● https://orcid.org/0000-0001-7258-770X
Marcelo Barraza-Alfaro ● https://orcid.org/0000-0001-6378-7873
Pietro Curone ● https://orcid.org/0000-0003-2045-2154
Ian Czekala ● https://orcid.org/0000-0002-1483-8811
Daniele Fasano ● https://orcid.org/0000-0003-4679-4072
Cassandra Hall ● https://orcid.org/0000-0002-8138-0425
Iain Hammond ● https://orcid.org/0000-0003-1502-4315
Jane Huang ● https://orcid.org/0000-0001-6947-6072
John D. Ilee ● https://orcid.org/0000-0003-1008-1142
Andrés F. Izquierdo ● https://orcid.org/0000-0001-8446-3026
Jensen Lawrence ● https://orcid.org/0009-0007-5371-3548
Giuseppe Lodato ● https://orcid.org/0000-0002-2357-7692
François Ménard ● https://orcid.org/0000-0002-1637-7393
Christophe Pinte ● https://orcid.org/0000-0001-5907-5179
Giovanni P. Rosotti ● https://orcid.org/0000-0003-4853-5736
Jochen Stadler ● https://orcid.org/0000-0002-0491-143X
Richard Teague ● https://orcid.org/0000-0003-1534-5186
Leonardo Testi ● https://orcid.org/0000-0003-1859-3070
David Wilner ● https://orcid.org/0000-0003-1526-7587
Andrew Winter ● https://orcid.org/0000-0002-7501-9801
Tomohiro Yoshida ● https://orcid.org/0000-0001-8002-8473

References

Andrews, S. M. 2020, ARA&A, 58, 483
Andrews, S. M., Huang, J., Pérez, L. M., et al. 2018, ApJL, 869, L41
Andrews, S. M., Wilner, D. J., Zhu, Z., et al. 2016, ApJL, 820, L40
Aota, T., Inoue, T., & Aikawa, Y. 2015, ApJ, 799, 141
Artur de la Villarmois, T., Guzmán, V. V., Yang, Y. L., Zhang, Y., & Sakai, N. 2023, A&A, 678, A124
Astropy Collaboration, Robitaille, T. P., Tollerud, E. J., et al. 2013, A&A, 558, A33
Bae, J., Isella, A., Zhu, Z., et al. 2023, in ASP Conf. Ser. 534, Astronomical Society of the Pacific Conference Series, ed. S. Inutsuka et al. (San Francisco, CA: ASP), 423
Bae, J., & Zhu, Z. 2018, ApJ, 859, 118
Benisty, M., Dominik, C., Follette, K., et al. 2023, in ASP Conf. Ser. 534, Protostars and Planets VII, ed. S. Inutsuka et al. (San Francisco, CA: ASP), 605
Benisty, M., Juhasz, A., Boccaletti, A., et al. 2015, A&A, 578, L6
Bi, J., Lin, M.-K., & Dong, R. 2021, ApJ, 912, 107
Binkert, F., Szulágyi, J., & Birnstiel, T. 2023, MNRAS, 523, 55
Boccaletti, A., Di Folco, E., Pantin, E., et al. 2020, A&A, 637, L5
Boehler, Y., Ricci, L., Weaver, E., et al. 2018, ApJ, 853, 162
Booth, A. S., Ilee, J. D., Walsh, C., et al. 2023a, A&A, 669, A53
Booth, A. S., Law, C. J., Temmink, M., Leemker, M., & Macías, E. 2023b, A&A, 678, A146
Booth, A. S., Leemker, M., van Dishoeck, E. F., et al. 2024a, AJ, 167, 164
Booth, A. S., Temmink, M., van Dishoeck, E. F., et al. 2024b, AJ, 167, 165
Booth, A. S., van der Marel, N., Leemker, M., van Dishoeck, E. F., & Ohashi, S. 2021, A&A, 651, L6
Booth, A. S., Walsh, C., Kama, M., et al. 2018, A&A, 611, A16
Bridle, A. H., & Schwab, F. R. 1999, in ASP Conf. Ser. 180, Synthesis Imaging in Radio Astronomy II, ed. G. B. Taylor, C. L. Carilli, & R. A. Perley (San Francisco, CA: ASP), 371
Briggs, D. S. 1995, PhD thesis, New Mexico Inst. of Mining and Technology
Brown, J. M., Herczeg, G. J., Pontoppidan, K. M., & van Dishoeck, E. F. 2012, ApJ, 744, 116
Calcino, J., Price, D. J., Hilder, T., et al. 2025, MNRAS, 537, 2695
Calcino, J., Price, D. J., Pinte, C., et al. 2019, MNRAS, 490, 2579

Casassus, S., & Cárcamo, M. 2022, MNRAS, 513, 5790
Casassus, S., Cárcamo, M., Hales, A., Weber, P., & Dent, B. 2022, ApJL, 933, L4
Clark, W. W., & De Lucia, F. C. 1976, JMoSp, 60, 332
Cleeves, L. I., Bergin, E. A., & Harries, T. J. 2015, ApJ, 807, 2
Codella, C., Podio, L., De Simone, M., et al. 2024, MNRAS, 528, 7383
Cornwell, T. J. 2008, ISTSP, 2, 793
Cridland, A. J., Lega, E., & Benisty, M. 2025, A&A, 693, A86
Curone, P., Facchini, S., Andrews, S. M., et al. 2025, ApJL, 984, L9
Czekala, I., Loomis, R. A., Teague, R., et al. 2021, ApJS, 257, 2
Debes, J. H., Poteet, C. A., Jang-Condell, H., et al. 2017, ApJ, 835, 205
Dong, R., Liu, S.-y., Eisner, J., et al. 2018, ApJ, 860, 124
Dong, R., Zhu, Z., Rafikov, R. R., & Stone, J. M. 2015, ApJL, 809, L5
Dutrey, A., Chapillon, E., Guilloteau, S., et al. 2024, A&A, 689, L7
Eistrup, C., Walsh, C., & van Dishoeck, E. F. 2016, A&A, 595, A83
Eriksson, L. E. J., Yang, C.-C., & Armitage, P. J. 2025, MNRAS, 537, L26
Evans, M. G., Hartquist, T. W., Caselli, P., et al. 2019, MNRAS, 483, 1266
Evans, M. G., Ilee, J. D., Boley, A. C., et al. 2015, MNRAS, 453, 1147
Facchini, S., Juhász, A., & Lodato, G. 2018, MNRAS, 473, 4459
Facchini, S., Teague, R., Bae, J., et al. 2021, AJ, 162, 99
Flores, C., Ohashi, N., Tobin, J. J., et al. 2023, ApJ, 958, 98
Follette, K. B., Grady, C. A., Swearingen, J. R., et al. 2015, ApJ, 798, 132
Follette, K. B., Rameau, J., Dong, R., et al. 2017, AJ, 153, 264
Fuente, A., Cernicharo, J., Agúndez, M., et al. 2010, A&A, 524, A19
Gaia Collaboration 2020, yCat, 1350, 0
Galloway-Sprietsma, M., Bae, J., Izquierdo, A. F., et al. 2025, ApJL, 984, L10
Gangi, M., Antoniucci, S., Biazzo, K., et al. 2022, A&A, 667, A124
Garcia Lopez, R., Natta, A., Testi, L., & Habart, E. 2006, A&A, 459, 837
Garg, H., Pinte, C., Christiaens, V., et al. 2021, MNRAS, 504, 782
Garg, H., Pinte, C., Hammond, I., et al. 2022, MNRAS, 517, 5942-5958
Garufi, A., Ginski, C., van Holstein, R. G., et al. 2024, A&A, 685, A53
Garufi, A., Podio, L., Codella, C., et al. 2022, A&A, 658, A104
Ginski, C., Facchini, S., Huang, J., et al. 2021, ApJL, 908, L25
Goldreich, P., & Tremaine, S. 1979, ApJ, 233, 857
Goldsmith, P. F., & Langer, W. D. 1999, ApJ, 517, 209
Gonzalez, J.-F., van der Plas, G., Pinte, C., et al. 2020, MNRAS, 499, 3837
Grady, C. A., Woodgate, B. E., Bowers, C. W., et al. 2005, ApJ, 630, 958
Grant, S. L., Espaillat, C. C., Brittain, S., Scott-Joseph, C., & Calvet, N. 2022, ApJ, 926, 229
Gray, R. O., Riggs, Q. S., Koen, C., et al. 2017, AJ, 154, 31
Gupta, A., Miotello, A., Manara, C. F., et al. 2023, A&A, 670, L8
Haffert, S. Y., Bohn, A. J., de Boer, J., et al. 2019, NatAs, 3, 749
Hall, C., Dong, R., Teague, R., et al. 2020, ApJ, 904, 148
Hammond, I., Christiaens, V., Price, D. J., et al. 2022, MNRAS, 515, 6109
Hammond, I., Christiaens, V., Price, D. J., et al. 2023, MNRAS, 522, L51
Harris, C. R., Millman, K. J., van der Walt, S. J., et al. 2020, Natur, 585, 357
Hartigan, P., & Kenyon, S. J. 2003, ApJ, 583, 334
Hartquist, T. W., Dalgarno, A., & Oppenheimer, M. 1980, ApJ, 236, 182
Hashimoto, J., Tamura, M., Muto, T., et al. 2011, ApJL, 729, L17
Hennebelle, P., Lesur, G., & Fromang, S. 2017, A&A, 599, A86
Herczeg, G. J., Chen, Y., Donati, J.-F., et al. 2023, ApJ, 956, 102
Herczeg, G. J., & Hillenbrand, L. A. 2014, ApJ, 786, 97
Hildebrand, R. H. 1983, QJRAS, 24, 267
Huang, J., Bergin, E. A., Bae, J., Benisty, M., & Andrews, S. M. 2023, ApJ, 943, 107
Huang, J., Andrews, S. M., Pérez, L. M., et al. 2018, ApJL, 869, L43
Huang, J., Bergin, E. A., Le Gal, R., et al. 2024, ApJ, 973, 135
Hunter, J. D. 2007, CSE, 9, 90
Ilee, J. D., Boley, A. C., Caselli, P., et al. 2011, MNRAS, 417, 2950
Hunter, T. R., Petry, D., Barkats, D., Corder, S., & Indebetouw, R. 2023, analysisUtils, Version 2.6, Zenodo, doi:10.5281/zenodo.7502160
Isella, A., Carpenter, J. M., & Sargent, A. I. 2010, ApJ, 714, 1746
Izquierdo, A. F., Facchini, S., Rosotti, G. P., van Dishoeck, E. F., & Testi, L. 2022, ApJ, 928, 2
Izquierdo, A. F., Stadler, J., Galloway-Sprietsma, M., et al. 2025, ApJL, 984, L8
Izquierdo, A. F., Testi, L., Facchini, S., et al. 2023, A&A, 674, A113
Jiang, H., Wang, Y., Ormel, C. W., Krijt, S., & Dong, R. 2023, A&A, 678, A33
Keppler, M., Benisty, M., Müller, A., et al. 2018, A&A, 617, A44
Keyte, L., Kama, M., Booth, A. S., et al. 2023, NatAs, 7, 684
Kratter, K., & Lodato, G. 2016, ARA&A, 54, 271
Kuffmeier, M., Calcutt, H., & Kristensen, L. E. 2019, A&A, 628, A112
Kuffmeier, M., Goicovic, F. G., & Dullemond, C. P. 2020, A&A, 633, A3
Kuo, I. H. G., Yen, H.-W., Gu, P.-G., & Chang, T.-E. 2022, ApJ, 938, 50
Kuznetsova, A., Bae, J., Hartmann, L., & Low, M.-M. M. 2022, ApJ, 928, 92
Law, C. J., Benisty, M., Facchini, S., et al. 2024, ApJ, 964, 190

Law, C. J., Booth, A. S., & Öberg, K. I. 2023, ApJL, 952, L19
Leemker, M., Booth, A. S., van Dishoeck, E. F., et al. 2022, A&A, 663, A23
Le Gal, R., Öberg, K. I., Loomis, R. A., Pegues, J., & Bergner, J. B. 2019, ApJ, 876, 72
Lesur, G., Flock, M., Ercolano, B., et al. 2023, in ASP Conf. Ser. 534, Protostars and Planets VII, ed. S. Inutsuka et al. (San Francisco, CA: ASP), 465
Lesur, G., Hennebelle, P., & Fromang, S. 2015, A&A, 582, L9
Long, F., Herczeg, G. J., Harsono, D., et al. 2019, ApJ, 882, 49
Long, F., Pinilla, P., Herczeg, G. J., et al. 2018, ApJ, 869, 17
Longarini, C., Lodato, G., Clarke, C. J., et al. 2024, A&A, 686, L6
Loomis, R. A., Facchini, S., Benisty, M., et al. 2025, ApJL, 984, L7
Luhman, K. L. 2023, AJ, 165, 37
Macías, E., Guerra-Alvarado, O., Carrasco-González, C., et al. 2021, A&A, 648, A33
Manara, C. F., Ansdell, M., Rosotti, G. P., et al. 2023, in ASP Conf. Ser. 534, Protostars and Planets VII, ed. S. Inutsuka et al. (San Francisco, CA: ASP), 539
Manara, C. F., Tazzari, M., Long, F., et al. 2019, A&A, 628, A95
Mesa, D., Ginski, C., Gratton, R., et al. 2022, A&A, 658, A63
Montesinos, M., Perez, S., Casassus, S., et al. 2016, ApJL, 823, L8
Mooley, K., Hillenbrand, L., Rebull, L., Padgett, D., & Knapp, G. 2013, ApJ, 771, 110
Nealon, R., Dipierro, G., Alexander, R., Martin, R. G., & Nixon, C. 2018, MNRAS, 481, 20
Öberg, K. I., & Bergin, E. A. 2021, PhR, 893, 1
Öberg, K. I., Facchini, S., & Anderson, D. E. 2023, ARA&A, 61, 287
Öberg, K. I., Guzmán, V. V., Walsh, C., et al. 2021, ApJS, 257, 1
Öberg, K. I., Murray-Clay, R., & Bergin, E. A. 2011, ApJL, 743, L16
Ohashi, S., Kataoka, A., van der Marel, N., et al. 2020, ApJ, 900, 81
Ono, T., Okamura, T., Okuzumi, S., & Muto, T. 2025, PASJ, 77, 149
Oya, Y., Saiga, E., Miotello, A., et al. 2025, ApJ, 980, 263
Pacheco-Vázquez, S., Fuente, A., Baruteau, C., et al. 2016, A&A, 589, A60
Padoan, P., Pan, L., Pelkonen, V.-M., Haugboelle, T., & Nordlund, A. 2025, NatAs, 9, 862
Paneque-Carreño, T., Pérez, L. M., Benisty, M., et al. 2021, ApJ, 914, 88
Pérez, L. M., Carpenter, J. M., Andrews, S. M., et al. 2016, Sci, 353, 1519
Pineda, J. E., Szulágyi, J., Quanz, S. P., et al. 2019, ApJ, 871, 48
Pinte, C., Teague, R., Flaherty, K., et al. 2023, in ASP Conf. Ser. 534, Protostars and Planets VII, ed. S. Inutsuka et al. (San Francisco, CA: ASP), 645
Podio, L., Tabone, B., Codella, C., et al. 2021, A&A, 648, A45
Rampinelli, L., Facchini, S., Leemker, M., et al. 2024, A&A, 689, A65
Reggiani, M., Christiaens, V., Absil, O., et al. 2018, A&A, 611, A74
Ren, B., Dong, R., Esposito, T. M., et al. 2018, ApJL, 857, L9
Ren, B., Dong, R., van Holstein, R. G., et al. 2020, ApJL, 898, L38
Ren, B. B., Benisty, M., Ginski, C., et al. 2023, A&A, 680, A114
Rivière-Marichalar, P., Fuente, A., Le Gal, R., et al. 2020, A&A, 642, A32
Safonov, B. S., Strakhov, I. A., Goliguzova, M. V., & Voziakova, O. V. 2022, AJ, 163, 31
Salyk, C., Herczeg, G. J., Brown, J. M., et al. 2013, ApJ, 769, 21
Schworer, G., Lacour, S., Huélamo, N., et al. 2017, ApJ, 842, 77
Semenov, D., & Wiebe, D. 2011, ApJS, 196, 25

Soderblom, D. R., Hillenbrand, L. A., Jeffries, R. D., Mamajek, E. E., & Naylor, T. 2014, in Protostars and Planets VI, ed. H. Beuther et al. (Tucson, AZ: Univ. Arizona Press), 219
Speedie, J., Dong, R., Hall, C., et al. 2024, Natur, 633, 58
Speedie, J., Dong, R., Teague, R., et al. 2025, ApJL, 981, L30
Stapper, L. M., Hogerheijde, M. R., van Dishoeck, E. F., & Mentel, R. 2022, A&A, 658, A112
Su, Z., & Bai, X.-N. 2024, ApJ, 975, 126
Tang, Y.-W., Dutrey, A., Guilloteau, S., et al. 2014, ApJ, 793, 10
Tang, Y.-W., Guilloteau, S., Dutrey, A., et al. 2017, ApJ, 840, 32
Teague, R. 2019, JOSS, 4, 1632
Teague, R. 2020, richteague/keplerian_mask: Initial Release, v1.0, Zenodo, doi:10.5281/zenodo.4321137
Teague, R., Bae, J., Andrews, S. M., et al. 2022, ApJ, 936, 163
Teague, R., Benisty, M., Facchini, S., et al. 2025, ApJL, 984, L6
Teague, R., & Foreman-Mackey, D. 2018, RNAAS, 2, 173
The CASA Team, Bean, B., Bhatnagar, S., et al. 2022, PASP, 134, 114501
Tripathi, A., Andrews, S. M., Birnstiel, T., & Wilner, D. J. 2017, ApJ, 845, 44
Ubeira Gabellini, M. G., Miotello, A., Facchini, S., et al. 2019, MNRAS, 486, 4638
Uyama, T., Muto, T., Mawet, D., et al. 2020, AJ, 159, 118
van Boekel, R., Henning, T., Menu, J., et al. 2017, ApJ, 837, 132
van der Marel, N., Birnstiel, T., Garufi, A., et al. 2021a, AJ, 161, 33
van der Marel, N., Booth, A. S., Leemker, M., van Dishoeck, E. F., & Ohashi, S. 2021b, A&A, 651, L5
van Gelder, M. L., Tabone, B., van Dishoeck, E. F., & Godard, B. 2021, A&A, 653, A159
van't Hoff, M. L. R., Tobin, J. J., Li, Z.-Y., et al. 2023, ApJ, 951, 10
Veronesi, B., Paneque-Carreño, T., Lodato, G., et al. 2021, ApJL, 914, L27
Vidal, T. H. G., Loison, J.-C., Jaziri, A. Y., et al. 2017, MNRAS, 469, 435
Vieira, S. L. A., Corradi, W. J. B., Alencar, S. H. P., et al. 2003, AJ, 126, 2971
Vioque, M., Oudmaijer, R. D., Baines, D., Mendigutìa, I., & Pérez-Martìnez, R. 2018, A&A, 620, A128
Virtanen, P., Gommers, R., Oliphant, T. E., et al. 2020, NatMe, 17, 261
Wagner, K., Leisenring, J., Cugno, G., et al. 2024, AJ, 167, 181
Wagner, K., Stone, J., Skemer, A., et al. 2023, NatAs, 7, 1208
Wagner, K., Stone, J. M., Spalding, E., et al. 2019, ApJ, 882, 20
Wichittanakom, C., Oudmaijer, R. D., Fairlamb, J. R., et al. 2020, MNRAS, 493, 234
Winter, A. J., Benisty, M., & Andrews, S. M. 2024, ApJL, 972, L9
Wölfer, L., Barraza-Alfaro, M., Teague, R., et al. 2025, ApJL, 984, L22
Wölfer, L., Facchini, S., Kurtovic, N. T., et al. 2021, A&A, 648, A19
Wölfer, L., Facchini, S., van der Marel, N., et al. 2023, A&A, 670, A154
Yamato, Y., Aikawa, Y., Ohashi, N., et al. 2023, ApJ, 951, 11
Yang, H., Fernández-López, M., Li, Z.-Y., et al. 2023, ApJL, 948, L2
Yen, H.-W., Koch, P. M., Liu, H. B., et al. 2016, ApJ, 832, 204
Yoneda, H., Tsukamoto, Y., Furuya, K., & Aikawa, Y. 2016, ApJ, 833, 105
Yoshida, T. C., Nomura, H., Law, C. J., et al. 2024, ApJL, 971, L15
Zhang, Z. E., Sakai, N., Ohashi, S., et al. 2024, ApJ, 966, 207
Zhu, Z., Dong, R., Stone, J. M., & Rafikov, R. R. 2015, ApJ, 813, 88
Zhu, Z., Zhang, S., & Johnson, T. M. 2025, ApJ, 980, 259
Ziampras, A., Dullemond, C. P., Birnstiel, T., Benisty, M., & Nelson, R. P. 2025, MNRAS, 540, 1185